NUMERICAL MODELING TOWARDS SIMULATIONS OF MULTIPHASE DETONATION TUBE EXPERIMENTS

A Thesis

by

BENJAMIN JOEL MUSICK

Submitted to the Graduate and Professional School of
Texas A&M University
in partial fulfillment of the requirements for the degree of

MASTER OF SCIENCE

Chair of Committee,	Jacob A. McFarland
Committee Members,	Eric L. Petersen
	Mark L. Kimber
Head of Department,	Guillermo Aguilar

August 2023

Major Subject: Mechanical Engineering

ABSTRACT

Multiphase detonations are phenomena involving multiple coupled systems evoking fundamental thermodynamic, hydrodynamic, heat/mass transfer, and chemical questions that require in depth analyses to provide insight into the what, where, when, why, and how of the complex process. Of particular interest in this work is the multiphase detonation phenomena involving wave propagation through liquid hydrocarbon fuel droplets and gaseous oxidizers. The success of a multiphase detonation in this context, from which the detonation strength and stability are of major interest, is dependent on the heat and mass transfer processes of the droplet in relation to the chemical burning time scales at play required for detonability. Fuel droplet heat and mass transfer under detonation conditions is driven primarily by evaporation and droplet breakup. With evaporation, breakup, and chemical burning occurring on similar time scales, a competition begins for which process will dominate properties of the detonation.

Multiphase detonations will be investigated from a numerical perspective. An open-source computational fluid dynamics code, FLASH, will be utilized for the analysis with the end result being full scale, two-dimensional simulations. This work aims to expand both on the code capabilities and comprehension of work done at the Texas A&M University Fluid Mixing at Extreme Conditions Laboratory. Global, single-step reactions will be expanded to a more general two-step formulation of an irreversible reaction ($C_nH_m + \left(\frac{n}{2} + \frac{m}{4}\right) O_2 \longrightarrow nCO + \frac{m}{2} H_2O$) paired with one reversible reaction ($CO + \frac{1}{2}O_2 \longleftrightarrow CO_2$) applicable for air combustion. Zero-dimensional model verification will be presented along with one- and two-dimensional results implemented into the FLASH code. Droplet vaporization will be investigated through a new model that examines different modes of burning and combines available reduced order models. Comparisons to previous work done with n-dodecane-oxygen detonations will be provided. The capabilities presented in this work lay the foundation for future multiphase detonation simulations capable of resolving spatial variance in equivalence ratio and different droplet burning regimes.

DEDICATION

To my coworker, gym partner, and friend, Hanif Zargarnezhad.

ACKNOWLEDGMENTS

I would like to take a moment to acknowledge the people who made it possible for me to make it this far in my career. Immediate thanks are due to my parents for creating me, raising me to be successful, and providing support for me. None of this would have been possible without United States of America taxpayers that inadvertently paid for my education and monthly stipend through U.S. Government grants during my time in graduate school. Hopefully I will contribute something useful to society to make this up to you. I relied on countless people for support in graduate school, those that immediately come to mind are my long term friends Mike, James, Cameron and Ethan. I would like to especially acknowledge my friend and coworker Vasco, who I truly believe I can talk to about anything and come away from the conversation wiser than going in.

Thank you to my first engineering manager Bob, who taught me how to practically approach engineering problems. Thank you to Jonathan and Cory who gave me footing in my first real engineering role. Special thanks are owed to Jeremy and Debbie from the same job who taught me an unbelievable amount of practical life lessons. Thank you to Trane Technologies for giving me an industry internship while in graduate school related to my field of study. Thanks are owed to Mitch, Alexis, and J. Curtis who continued to further my understanding of practical applied engineering. While at that job I met several people that changed my perspective on graduate school and life. Shout out to Logan, Nick, Stinky Binky, and Rob.

Thanks are owed to the community surrounding the open-source hydrodynamics code FLASH, developed in part at the Flash Center for Computational Science, maintained over the years by various University of Chicago and Rochester staff.

The computation for this work was performed in part on the high performance computing infrastructure provided by Research Support Solutions and in part by the National Science Foundation under grant number CNS-1429294 at the University of Missouri, Columbia MO. Portions of this research were conducted with the advanced computing resources provided by Texas A&M High Performance Research Computing.

CONTRIBUTORS AND FUNDING SOURCES

Contributors

This work was supported by a thesis committee consisting of Professor Jacob A. McFarland and Eric L. Petersen of the Department of Mechanical Engineering and Professor Mark L. Kimber of the Department of Nuclear Engineering. Consultation and collaboration with Manoj Paudel of the Department of Mechanical Engineering was additionally instrumental in the completion of this thesis.

Consultation and feedback on various research aspects were received from Professor Praveen Ramaprabhu and Prashant Tarey at the University of North Carolina at Charlotte.

All other work conducted for the thesis was completed by the student independently.

Funding Sources

Graduate study was supported by research grants from the National Science Foundation (NSF-2044767) and the Office of Naval Research (N00014-20-1-2796).

NOMENCLATURE

Units

$[cm]$	Centimeter, length
$[dyn]$	Dyne, force
$[erg]$	Erg, energy
$[cal]$	Calorie, energy
	1 $[cal]$ = 41868000 $[erg]$
$[g]$	Gram, mass
$[K]$	Kelvin, temperature
$[P]$	Poise, dynamic viscosity
$[s]$	Second, time

Notation

plain font	Scalar quantity
bold font	Vector or matrix quantity
$\lvert \cdot \rvert$	Magnitude
$\overline{overline}$	Averaged quantity
$\dot{dot}$	Rate quantity, time derivative, $\frac{[--]}{s}$
$\tilde{\mathbf{1}}$	Identity matrix

Latin Symbols & Abbreviations

a	Acceleration, $[cm/s^2]$
	Speed of sound, $[cm/s]$
	NASA polynomial coefficient
A	Area, $[cm^2]$
B	Heat/Mass transfer number
c_d	Drag coefficient
C	Specific heat capacity, $[\frac{erg}{g-K}]$
	TAB model coefficients
CJ	Chapman–Jouguet
d	Diameter, $[cm]$
$\mathcal{D}$	Binary diffusion coefficient, $[cm^2/s]$
E_a	Activation energy, $[cal/mol]$
EoS	Equation of State
g	Specific Gibbs free energy, $g = h - Ts$, $[erg/g]$
GCI	Grid Convergence Index
h	Specific enthalpy, $[erg/g]$
h_c	Convective heat transfer coefficient, $[\frac{erg}{s-cm^2-K}]$
h_{cf}	Convective mass transfer film coefficient, $[\frac{cm}{s}]$
IPM	Induction Parameter Model
J	Jacobian matrix
K	Equilibrium constant
KH	Kelvin-Helmholtz
LHV	Lower Heating Value

m	mass, $[g]$
Ma	Mach number
M	Third body species
MW	Molecular weight, $[g/mol]]$
n	Moles, $[mol]$
P	Pressure $[dyn/cm^2]$
P_{atm}	Pressure $[atm]$
	1 $[atm]$ = 1013250 $[dyn/cm^2]$
q	Heat transfer $[erg]$
r	Radius $[cm]$
$\mathcal{R}$	Universal gas constant, 8.31446261815324e7 $[\frac{erg}{mol-K}]$
$\mathcal{R}_c$	Universal gas constant, 1.98720425864083 $[\frac{cal}{mol-K}]$
R_g	Specific gas constant, $\mathcal{R}/MW$ $[\frac{erg}{g-K}]$
RT	Rayleigh-Taylor
s	specific entropy, $[erg/g-K]$
t	time, $[s]$
u	specific internal energy, $[erg/g]$
$u,\ v$	Velocity, $[cm/s]$
vN	von Neumann
X	Mole fraction
Y	Mass fraction
ZND	Zel'dovich-von Neumann-Doering

Superscripts

^{o}	Molar quantity
^{0}	Reference property
*	Modified parameter

Subscripts

C	Combustion
CJ	Property at the Chapman-Jouguet state/condition
d	Droplet property
f	Liquid phase property
F	Fuel vapor property
g	Gas phase property
$i,\ j$	Component index, usually in reference to species
M	Mass transfer quantity
p	Constant pressure property
r	Relative property, e.g. relative velocity U_r
s	Surface or constant entropy property
st	Stoichiometric
T	Thermal transport / heat transfer quantity
v	Constant volume property
0	Initial property

Nondimensional Numbers

Eo	Eötvös Number, $\frac{\Delta \rho a r^2}{\sigma}$
Le	Lewis Number, $\frac{\lambda_g}{\rho_g \mathcal{D} C_{p,g}}$
Nu	Nusselt Number, $\frac{h_c d}{\lambda}$
Oh	Ohnesorge Number, $\frac{\mu}{\sqrt{\rho \sigma d}}$
Pr	Prandtl Number, $\frac{C_p \mu}{\lambda}$
Re	Reynolds Number, $\frac{\rho v d}{\mu}$
Sc	Schmidt Number, $\frac{\mu}{\rho \mathcal{D}}$
Sh	Sherwood Number, $\frac{h_{cf} d}{\mathcal{D}}$
We	Weber Number, $\frac{\rho v^2 d}{\sigma}$

Greek Letters

(lowercase)

γ	Adiabatic index, for ideal gas $\frac{C_p}{C_v}$
ϵ	Error tolerance, void fraction
θ	Effective activation energy
κ	Reaction rate constant
λ	Thermal conductivity, $[\frac{erg}{s-cm-K}]$
μ	Dynamic viscosity, $[P]$
	Statistical mean
ν'	Stoichiometric coefficient matrix for reactants $[mol]$

ν''	Stoichiometric coefficient matrix for products, $[mol]$
ν	$\nu'' - \nu'$
π	Mathematical constant pi, 3.1415926535897932384
ρ	Density, $[\frac{g}{cm^3}]$
σ	Surface tension, $[\frac{dyn}{cm}]$
	Standard deviation
ς	Fuel to oxidizer ratio by mass, $[\frac{n_F MW_F}{n_o MW_o}]$
τ	Nondimensional or characteristic time
ϕ	Equivalence ratio, $(Fuel : Air)/(Fuel : Air)_{st}$
ψ	Function utilized in the Abramzon-Sirignano vaporization model, $\left[\frac{\overline{C}_{p,F}}{\overline{C}_{p,g}}\right]\left[\frac{Sh^*}{Nu^*}\right]\frac{1}{Le}$

(uppercase)

Δ	Change in variable
Π	Product operator
Σ	Summation operator

TABLE OF CONTENTS

Page

LIST OF FIGURES

FIGURE Page

LIST OF TABLES

TABLE Page

1. INTRODUCTION AND LITERATURE REVIEW

1.1 Low vs. High Speed Combustion

Combustion can usually be described as a rapid chemical process, e.g. oxidation, that produces heat and light.[1] This is a good starting point for the discussions to follow. We will dissect and concern ourselves with the following elements from the definition: "rapid," "oxidation," and "produces heat." Rapid is rather subjective depending on what type of combustion application is under review. HVAC furnaces can rapidly achieve steady-state operation within minutes of operation. Detonations can rapidly travel meters within milliseconds. Oxidation is the fundamental underlying process in hydrocarbon combustion, with the global mechanism $C_nH_m + (n + m/2)O_2 \rightarrow nCO_2 + (m/2)H_2O$ usually being the first introduction people have to burning. Heat production is likely the most nuanced aspect of combustion, having strong dependence on the system and thermodynamic process at play. Heat is energy, and energy is needed for everything producing work. The type of work desired, such as conditioning air vs. propulsion, will dictate how this energy is manipulated.

Most combustion we encounter in everyday life is low speed, e.g. gasoline engines, butane lighters, or natural gas appliances. Combustion processes occurring at low speeds are often well characterized due to the ability to observe, reproduce, and collect data at speeds well within the capabilities of most equipment commercially available. High speed, unsteady processes such as detonations provide considerable difficulty when it comes to the ability to observe, reproduce, and collect high quality information. There are many aspects of high speed combustion that can both create dangers to humanity but also provide opportunities for high energy yield devices. What is examined in this work is high speed combustion, most easily defined by reactions occurring at velocities greater than the speed of sound.

[1] https://www.merriam-webster.com/dictionary/combustion

1.2 Detonations

There has long been an effort to better understand explosive processes and how their power might be efficiently harvested. For example, detonations provide an opportunity for higher efficiency combustion cycles such as Pulse and Rotating Detonation Engines (PDE and RDE), which can be used for both power generation and propulsion [4]. The propagation of detonation waves in gaseous media is relatively well studied but there are still many gaps in the overall understanding of the process, especially when it comes to the Deflagration-to-Detonation Transition (DDT) or the stability/structure of a traveling wave.

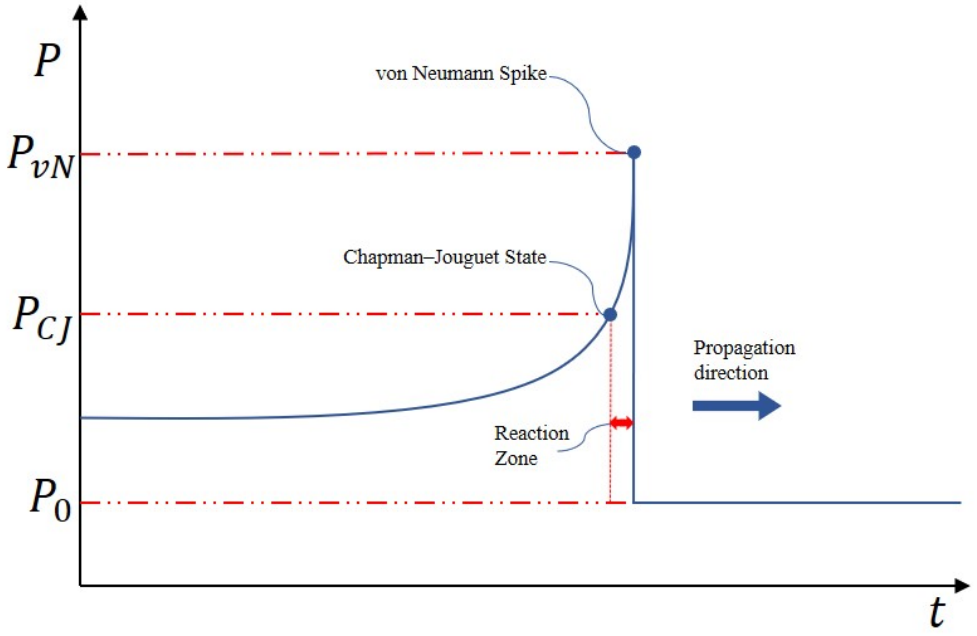

Figure 1.1: Pressure profile of a CJ detonation over time in a confined tube.

The majority of what is known about detonations has been obtained through the study of homogeneous gas-phase mixtures of fuel and oxidizer, usually some H_2-O_2-Ar media. Early zero-dimensional analysis was theorized by Chapman [5] and Jouguet [6, 7]. The one-dimensional theory of detonations was independently derived by Zel'dovich (Z) [8], von Neumann (N) [9],

and Döring (D) [10] which describes a purely 1D detonation structure (the ZND model). Both models are a good starting points for determining the expected bulk properties of a detonation. Real, observed detonations are known to differ from the models quite considerably, having an inherent three dimensional structure, often called a cellular structure, sometimes simply "cells," or a multi-head structure. There has been a considerable amount of work done both experimentally and numerically to characterize these structures, such as [11] or [12]. Further, real detonations can undergo transient modes of repeated over- and under-driven conditions.

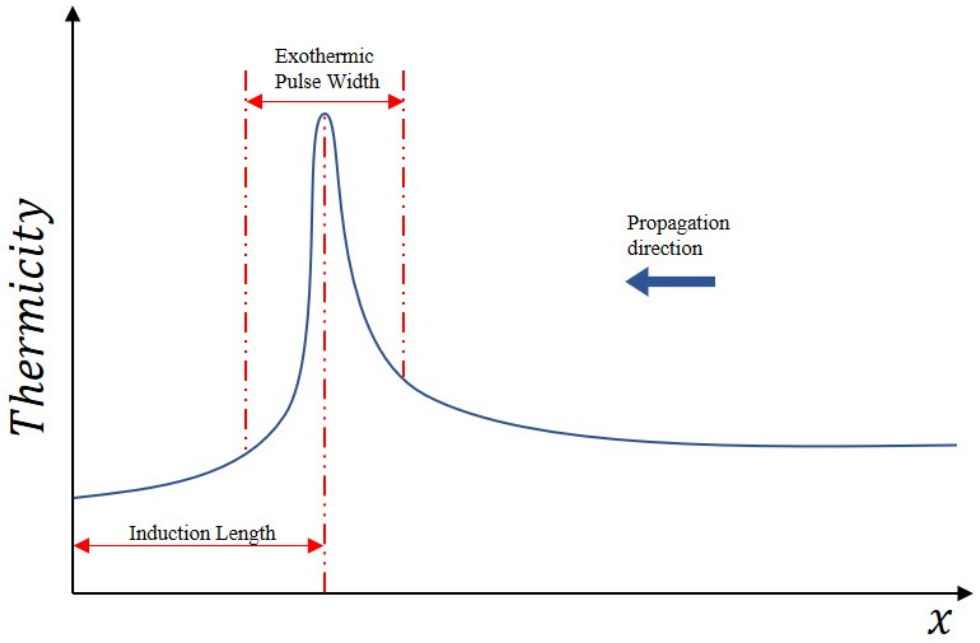

Figure 1.2: Induction length and exothermic pulse width diagram. Induction length and exothermic pulse width are two defining features of the ZND detonation profile.

The key fundamentals of the reduced models are still close enough to the real process that they are helpful for many aspects of understanding how detonations propagate. The CJ structure of the detonation wave assumes a shock front moving at speed D_{CJ}, the immediate post shock properties of which determine the pressure known as the von Neumann spike, which is then followed by a series of expansions. The CJ detonation wave runs under the assumption that the post shock

properties are of sufficient temperature to kickoff reactions which then sustain the detonation wave front. Reactions are assumed to complete at or before the local Mach number in reference to D_{CJ} is equal to one, the point which is referred to as the CJ state. The ZND model extends the understanding of this model to one spatial dimension, identifying two fundamental structures of the 1D detonation wave: the induction length and the exothermic pulse width. The induction length is the location behind the shock front where thermicity (a measure of instantaneous heat release) is of peak value. The exothermic pulse width is the region centered around this peak where heat release occurs. Further details of the detonation phenomena can be found in great detail in [13].

1.2.1 Gaseous Fuels

The view of detonations taken in this work, and several others such as [14, 15, 16, 17], is heavily influenced by the perspectives and lessons learned by the gaseous detonation community. Gaseous detonations have received great attention from both experimental and numerical points of view. A good overview of gaseous detonations can be found in [18]. Detonations are both hydrodynamically and chemically complex, requiring investigation techniques from multiple scientific backgrounds. Experimental quantification of a gaseous detonation is usually conducted through a series of pressure transducer measurements and/or optical techniques. Dynamic pressure transducers can be arranged along a shock/detonation tube in measured increments to compute average propagation velocities, sometimes being able to resolve pressures in the detonation wave front, often near the expected CJ pressure. One of the more coveted measurements often reported in gaseous detonation works is the cellular structure of the detonation wave. There are a handful of ways to obtain such measurements, but soot/smoke foil techniques are most commonly seen in literature, utilizing an aluminum sheet coated with soot from kerosene combustion placed on an inner wall of the test chamber. The soot is deformed as high pressure waves travel over the plate, capturing the time integrated dynamics of the wave front. Simulation studies will often use this type of information for code validation. Numerical smoke foils can be easily generated by recording the maximum pressure in each computational cell at each time step. Additional optical techniques, such as Schlieren and Planar Laser-Induced Fluorescence, can be used to quantify detonations by

the detection of wave fronts and species concentrations.

1.2.2 Condensed Phase Reactants

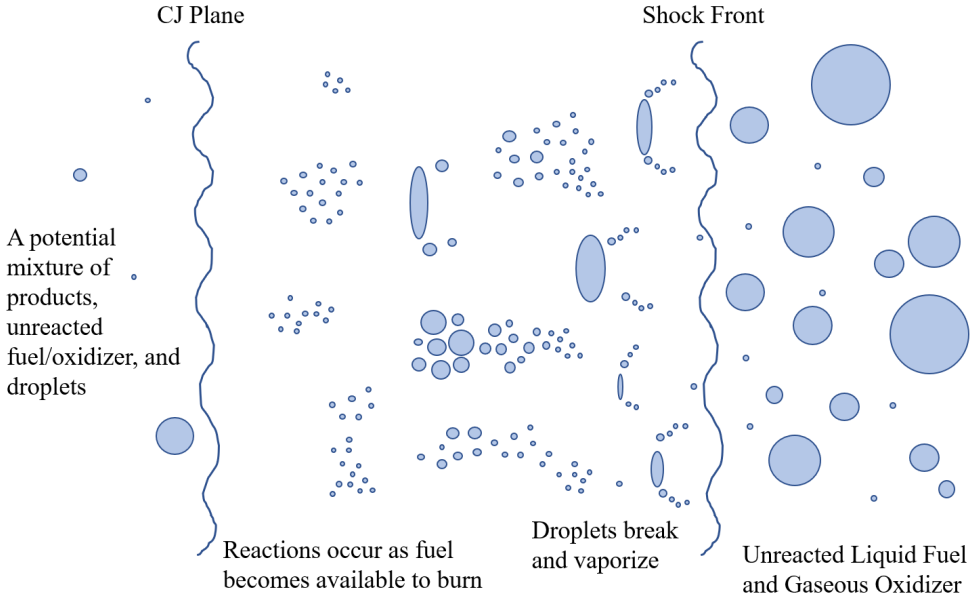

Figure 1.3: An illustration of the general multiphase detonation process where fuel is supplied in the liquid phase.

The less studied multiphase detonation phenomena is not unlike the gaseous detonation in many ways, especially in the context of condensed hydrocarbon fuels. Fuels that are liquid at room temperature and atmospheric pressures have been heated in countless studies for gas phase detonation analysis, such as [19, 20]. The next level of complexity added by the multiphase detonation problem is what happens when pre-vaporization has not occurred, either partially (high vapor pressure fuels) or essentially not at all (low vapor pressure fuels). The next added level of complexity to the multiphase detonation phenomena is the shock-droplet interaction and evolution. This is where the multiphase system starts to lose direct comparisons to the CJ or ZND detonation wave models. Consider the illustration seen in Figure 1.3, where a liquid fuel and gaseous oxidizer lie in quiescent, non-reacting conditions. As the shock front passes over liquid droplets, they undergo deformation, breakup, and evaporation in addition to complex transport dependent

on the wave structure. Throughout this process as vapor begins to diffuse/advect away from the droplet, combustion has the opportunity to occur given sufficient mixing of reactants has taken place. Suddenly, there is no well defined reaction zone as it becomes dependent on the where, when, and how burning is occurring during the mass transfer process. Additionally, while the CJ plane certainly exists, the conditions at that point cannot be definitively pinned down for the heterogeneous process. Depending on the studied system, there could be a combination of droplets, unreacted fuel/oxidizer, and/or products. A more comprehensive history of multiphase detonations can be found in [21].

1.2.3 Experimental Studies

Work done with high vapor pressure fuels, e.g. [22, 23, 24], has shown that detonability is achievable given sufficient initiation energy is supplied. Low vapor pressure fuels present an unclear story, largely limited by differing experimental results and low publication volume. The studies conducted in [25, 26, 16] reveal regimes of either complete detonation failure or unstable wave modes. The investigations in [27, 28, 29, 30] provide a different story, generally reporting successful detonations in the conditions studied, albeit subject to propagation instability, or requiring a minimum ignition energy, dependent on test apparatus geometry, to yield detonations. The objective of the facility built at the FMECL [31] is to characterize the low vapor pressure fuel detonation regimes with greater detail, with a focus on droplet morphology in a detonation environment. Low vapor pressure fuels are of primary interest as many aviation fuels have a low vapor pressure. Currently, work is being conducted with the alkane n-dodecane which is the primary motivation for the numerical progress made in [17] and in this work.

1.2.4 Numerical Modeling

There is a long history of multiphase detonation modeling, often with large gaps in between each resurgence of interest in the phenomena. Some of the earliest work was conducted in one-dimension by [32, 33, 34, 35]. More recent works have extended modeling to two and three dimensions [14, 36, 16, 26, 24, 37, 15, 38, 39, 40, 41, 42, 43, 44, 17]. All of these simulations attempt

to resolve the macro-scale features of multiphase detonation propagtion, some even investigating more complex systems consistent with RDE geometries. For any two-phase flow simulation, the choice made for droplet modeling is largely dependent on what physical results are desired from the simulation. For these types of studies, gas hydrodynamics are often resolved in an Eulerian formulation while the models used for droplets can vary. Computational cost, not to mention numerical complexity, often prohibits resolving each droplet and its full set of governing physical equations. Two common methods employed to simply the liquid phase physics are Euler and Lagrangian formulations for the dispersed phase. Eulerian formulations treat the droplets as a continuous fluid of constant bulk properties. Additional source terms are added to achieve two-way coupling effects, e.g. momentum (droplet drag) or mass (vapor production). Lagrangian methods (employed in this work) resolve the dispersed phase as discrete points, each with the capability of unique properties, e.g. the ability to have different droplet diameters. Lagrangian methods require source terms for mass, momentum, and energy interpolated between the continuous and discrete meshes to achieve two-way coupling between the Eulerian gas mesh and Lagrangian particle points.

1.3 Discrete Phase Modeling (Lagrangian Point Modeling)

Euler-Lagrange methods are heavily reliant on reduced order modeling for the dispersed phase. The reduced models are used for source term coupling between the two phases, thus, a model with low confidence cannot be trusted to provide physical source terms and resolve the macro-scale hydrodynamics of the problem accurately. Both theoretical and empirical formulations can be utilized for such modeling, with a combinations of both often being employed. For instance, empirical drag models can be utilized for spherical droplets, however, during deformation under strong convective forces analytical models such as the Taylor Analogy Breakup (TAB) model [45] can be used to predict the displacement of the sphere to an ellipsoid and drag coefficients can be re-weighted accordingly.

Many fundamental models for discrete, dispersed spheroids can be found in reference texts such as [46, 47], however, the majority of models are restricted to specific flow regimes or assumptions about which physics are occurring. For instance, very basic droplet evaporation models

often neglect convection, pressure dependence, and the potential for reactions to occur. Generally speaking, there is not one model that will provide accurate results over a wide range of free stream conditions. Specific models are often developed with a particular set of physics in mind, such as evaporating fuel droplets in convective conditions [48] or breaking droplets in low Weber number post-shock conditions [49]. As models are constantly being reworked for particular physical problems, investigations such as [50, 51, 52, 53, 54] become increasingly important as many models become reliant on experimental data to tune constants for optimal performance across many subjected free stream conditions.

1.3.1 Breakup

Droplet breakup is a phenomena that has been well studied for many different regimes over the years. Breakup is a driving force in vaporization and thus a major modifier of droplet life expectancy. Breakup is a complex phenomena with several theories for how exactly a droplet undergoes this process. Theories such as proposed in [55, 56] directly attribute the phenomena to a combination of Rayleigh-Taylor (RT, acceleration driven) and Kelvin-Helmholtz (KH, shear driven) instabilities. Current theories vary, but more generally breakup is attributed to shearing forces, sometimes referred to as Shear-Induced Entrainment (SIE), and acceleration driven forces, Rayleigh-Taylor Piercing (RTP), experimental evidence of both modes can be seen in [57]. The regimes at which modes dominate breakup are debated [58, 59]. There are a wide variety of breakup models available, both theoretical and empirical, but both methods usually rely on flow characterization by some combination of Weber (inertial to surface tension forces), Ohnesorge (viscous forces to inertial and surface tension forces), or Eötvös (acceleration to surface tension forces) numbers.

The study conducted in [17] examined both an empirical breakup model (WERT49, [52]) and a theoretical model (KHRT, [55, 56]) to compare the effect each had on multiphase detonation modeling. The WERT49 breakup model was tuned to low speed shock tube data that sets the particle radius on an exponential decrease to match a predicted final child droplet radius. The KHRT model attempts to predict the fastest growing KH and/or RT instabilities on the droplet,

continuously shedding child droplets from KH modes and instantaneously breaking the parent droplet into many children in RT modes. The breakup and droplet life times predicted for the WERT49 model were one to two orders of magnitude slower than those predicted by the KHRT model, yielding very different results when utilized in a multiphase detonation simulation. The WERT49 model predicted various propagation deficits with a trend of decreasing speeds with increasing droplet size. The KHRT model predicted a deficit, but it was very small in comparison to the gaseous detonation and largely insensitive to droplet size. Of course, the largest contrast seen was simply the inclusion of a breakup model; detonation failures were observed for droplet sizes of 10 $[\mu m]$ and above. Thus the inclusion of a breakup model is deemed essential for accurate modeling of multiphase detonations. This work employs the WERT49 model as it is believed to have reasonable breakup times as seen in [52, 53].

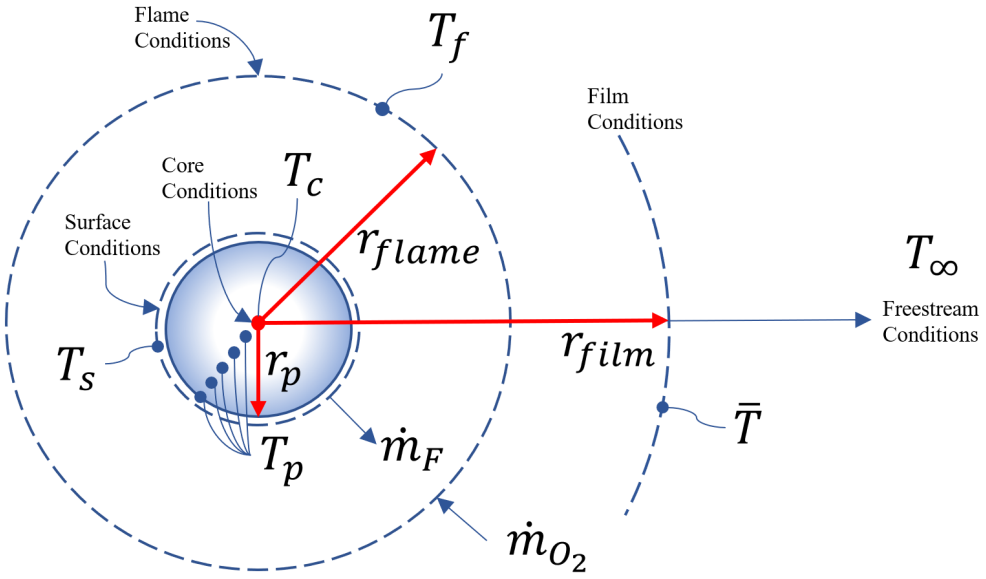

Figure 1.4: Free body diagram of a burning fuel droplet, depicting the many locations of potential physical importance.

1.3.2 Evaporation and Combustion

Reduced order heat and mass transfer modeling is heavily reliant on assumptions made about the droplet. As seen in the free body diagram in Figure 1.4, there are many states in between the droplet core and the free stream conditions, the distance to which is not well defined. Computational analysis often assumes free stream conditions to be an assumed constant value or, in the context of discrete modeling, an interpolation to the gas mesh where a particle is located is often utilized for free stream conditions. Fir the analysis conducted in this work, the assumption is made that the temperature distribution of the droplet is constant, i.e. there is no variation in temperature between the core and surface conditions. Evaporation is potentially both a diffusion and convection dominated problem, with the vapor production rate being dependent on the conditions in the droplet all the way out to the free stream. Thus, property evaluations are often made at both or a combination of each condition. The combination of the properties is referred to as a film condition that more accurately weights the effect of a state difference in between the droplet and free stream.

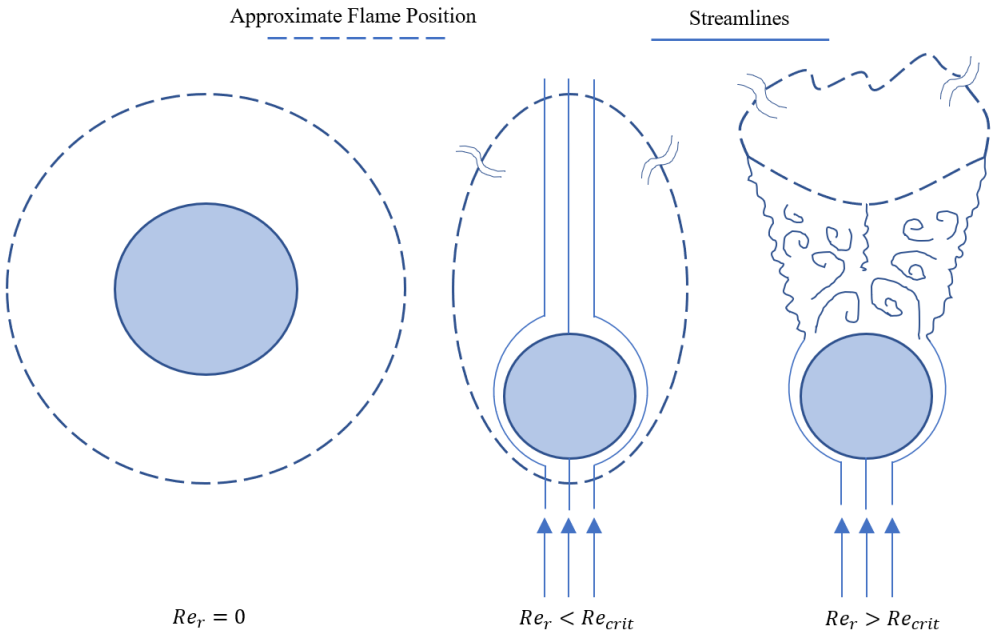

Figure 1.5: Approximate flame shapes for different flow conditions around a droplet.

The presence of a flame near the droplet is often not taken into account in vaporization models. Early models [60] implement boundary conditions to make the evaporation rate aware of oxidizer concentrations and heat release, however, feedback from the flame itself never seems to enter the model via film temperature re-weighting. Depending on the exact implementation, the effects of combustion will be incorporated into the transient heating of the drop. Additionally, simple models usually run under the assumption of infinitely fast kinetics occurring throughout the lifetime of the drop without an ignition source/delay incorporated. Further complicating matters is the flame shape around the droplet, which may not even be present under convective conditions as found experimentally in works such as [61, 62] and numerically in [63]. The flame structures can be generalized into three states as suggested in [63, 64], visualized in Figure 1.5. Envelope flames, as the name implies, envelop the entire droplet. Boundary layer flames are partially attached to the droplet at some point in the boundary layer around the droplet, varying in position from near the stagnation point or extreme positions near the equators. Wake flames are burning purely in the downstream wake of the droplet, during which vaporization is likely ignorant of combustion as suggested in [63, 64]. This work attempts to inform the evaporation rate of combustion, or lack thereof, under appropriate conditions through the combination of reduced order models. A detailed review of droplet evaporation/combustion modeling can be found in [65].

2. NUMERICAL METHODS AND MODELING[1]

The open-source FLASH hydrodynamics framework was utilized for the simulations presented in this work; developed in part at the Flash Center for Computational Science [66]. The FLASH code offers features such as Adaptive Mesh Refinement (AMR, PARAMESH [67]) and particle-to-gas property mapping between Euler and Lagrange meshes. More information can be found on the FLASH website.[2]

2.1 Computational Fluid Dynamics Implementation

An approach similar to the Multi-Phase Particle-In-Cell (MP-PIC) method [68, 69] is used for the implementation of particles. MP-PIC represents particles as Lagrangian points on an Eulerian mesh and interpolates properties between them. The conservation equations for the gas flow and particle motion are solved independently but linked with source terms to provide two-way coupling. Examples of this implementation in FLASH can be seen in [70, 52, 17]. The numerical methods utilized in this work follow that of [17], with minor modifications to source term models for different physics. The conservation equations are solved without source terms, then particles are advanced using sub-stepping (smaller time steps), and finally, the source terms are calculated, and the gas properties are updated. Source terms are handled through operator splitting. The FLASH code is setup to solve the Euler equations for gas flow with modular source terms as seen in Equations 2.1, 2.2, & 2.3,

$$\frac{\partial \epsilon \rho_g}{\partial t} + \nabla \cdot \epsilon \rho_g \mathbf{v}_g = -\dot{M}_p \tag{2.1}$$

$$\frac{\partial \epsilon \rho_g \mathbf{v}_g}{\partial t} + \nabla \cdot \epsilon \rho_g \mathbf{v}_g \mathbf{v}_g + \nabla P = -\mathbf{F}_p \tag{2.2}$$

$$\frac{\partial \epsilon \rho_g E}{\partial t} + \nabla \cdot (\epsilon \rho_g E + P)\mathbf{v}_g + \frac{P \partial \epsilon}{\partial t} = \dot{E}_p + \dot{E}_{rxn} \tag{2.3}$$

[1] Parts of this chapter are reprinted with permission from [17].

[2] https://flash.rochester.edu/site/index.shtml

where the subscripts g and p denote gas and particle properties respectively, ϵ is the gas void fraction, ρ is density, t is time, $\mathbf{v}$ is velocity, P is pressure, and E is energy. $\dot{M}_p$, $\mathbf{F}_p$, and $\dot{E}_p$ are the mass, momentum, and energy source terms from the particle phase, respectively.

Reaction energy source terms are only necessary when using a calorically perfect EoS. When using a thermally perfect EoS that has energy as a function of temperature, changes in species composition with appropriate EoS subroutine calls will capture the change in temperature associated with reactions. Tracking multiple species in our simulation, with some that evaporate and others that react requires the addition of Equation 2.4,

$$\frac{\partial \epsilon \rho_g Y_i}{\partial t} + \nabla \cdot \epsilon \rho_g Y_i \mathbf{v}_g = -\dot{M}_{p,i} + \dot{M}_{rxn,i} \quad , \quad \sum_{i=1}^{n} Y_i = 1 \tag{2.4}$$

where Y is a mass fraction, $\dot{M}_{rxn}$ is the reacting species' mass consumption or production rate, and the subscript i represents each species in the simulation. $\dot{M}_{p,i}$ and $\dot{M}_{rxn}$ are zero for non-evaporating and non-reacting species, respectively. The gas equations are solved in a finite volume approach using directional splitting and a higher-order Godunov method (PPM [71]) for data reconstruction which yields good accuracy at discontinuities.

The Lagrangian particle system is solved using the Liouville equation for the particle distribution function, h, as seen in Equation 2.5:

$$\frac{\partial h}{\partial t} + \nabla \cdot (h \mathbf{v}_p) + \nabla \mathbf{v}_p \cdot (h \mathbf{a}_p) = 0 \tag{2.5}$$

Where $\mathbf{a}_p$ is the acceleration of the particles and is given by Equation 2.6:

$$\mathbf{a}_p = \frac{d\mathbf{v}_p}{dt} = \mathrm{f}_D(\mathbf{v}_g - \mathbf{v}_p) - \frac{1}{\rho_p} \nabla P \tag{2.6}$$

For this study, inter-particle stress terms are neglected. Interparticle spacing, l/d_p, is approximately 10 for an equivalence ratio of 1, under the assumption of pure oxygen combustion, which means individual droplets can be treated as isolated. Additionally, gravity for both gas and particle

motion is not incorporated as its contribution would be negligible over the time scales considered here. The scalar drag component, f_D, is evaluated as seen in Equation 2.7:

$$\mathrm{f}_D = C_d \frac{3}{8} \frac{\rho_g}{\rho_p} \frac{|\mathbf{v}_g - \mathbf{v}_p|}{r_p} \tag{2.7}$$

where C_d is the coefficient of drag, and r_p is the current particle radius. We consider two different models for the calculation of C_d for non-deforming and deforming particles. For a non-deforming, spherical particle, the coefficient of drag is determined from Equation 2.8:

$$C_{d,sph} = \begin{cases} \frac{9}{2} \frac{\mu_{g,\infty}}{r^2 \rho_p} & Re \leq 0.1 \\ \frac{24}{Re}(\epsilon^{-2.65} + \frac{Re^{2/3}}{6}\epsilon^{-1.78}) & 0.1 < Re < 1000 \\ 0.424 & 1000 \leq Re \end{cases} \tag{2.8}$$

where $\mu_{g,\infty}$ is the free-stream dynamic viscosity, and Re is the Reynolds number evaluated at the free stream conditions, $Re = \rho_{g,\infty}|\mathbf{v}_g - \mathbf{v}_p|2r_p/\mu_{g,\infty}$. Deformation is calculated by solving the second-order equation for droplet surface oscillation as given by the TAB model [45], Equation 2.9,

$$\frac{d^2y}{dt^2} = \frac{C_f \rho_g |\mathbf{v}_g - \mathbf{v}_p|^2}{C_b \rho_p r_p^2} - \frac{C_k \sigma}{\rho_p r_p^3} y - \frac{C_\delta \mu_p}{\rho_p r_p^2} \frac{dy}{dt} \tag{2.9}$$

where y is the non-dimensional deformation equal to $x/(C_b r_p)$ (x = displacement of droplet equator from its undisturbed position), C_f, C_k, C_b and C_δ are constants, μ_p is the liquid dynamic viscosity and σ the liquid surface tension. Based on the calculated deformation, the coefficient of drag is evaluated as the weighted average of a non-deforming sphere and a disk (see [17] for additional details).

2.2 Gas Phase Thermodynamics

The EoS often used in the FLASH code is the calorically perfect ideal gas law, which in general obeys the following thermodynamic relations,

$$\begin{aligned} P &= \rho R_g T \\ P &= \rho u(\gamma - 1) \\ u &= C_v T \\ R_g &= C_p - C_v \\ R_g T &= h - u \end{aligned} \tag{2.10}$$

With the implementation of NASA7 thermodynamics into FLASH, the specific heat capacities, energy, and entropy are now polynomial functions of temperature, making the formulation thermally perfect,

$$\begin{aligned} \frac{C_p}{R} &= a_1 + a_2 T + a_3 T^2 + a_4 T^3 + a_5 T^4 \\ \frac{h}{RT} &= a_1 + \frac{a_2}{2} T + \frac{a_3}{3} T^2 + \frac{a_4}{4} T^3 + \frac{a_5}{5} T^4 + \frac{a_6}{T} \\ \frac{s}{R} &= a_1 \ln(T) + a_2 T + \frac{a_3}{2} T^2 + \frac{a_4}{3} T^3 + \frac{a_5}{4} T^4 + a_7 \end{aligned} \tag{2.11}$$

The coefficients appearing in the polynomial form are usually split between a low and high temperature range for the NASA7 format. FLASH subroutines tend to favor using calls to the EoS where density, internal energy, and species mass fractions are input as known quantities. This creates additional work in the form of a bisection or Newton-Raphson iteration for temperature. Convergence is usually met rather quick (<5 iterations) when employing a Newton-Raphson method as long as the polynomials are relatively smooth and do not have large discontinuities between their different temperature ranges.

2.3 Gas Phase Reactions

The Induction Parameter Model (IPM) and Arrhenius rate model differ significantly when it comes to theory and implementation. For the discussions to follow, it is important to remember that the implementation of IPM in FLASH was designed around the calorically perfect EoS while the Arrhenius rate models rely heavily on the thermally perfect EoS.

There are several different methods to model chemical reactions in simulations with varying degrees of complexity and usually specific applications in mind. Detonation modeling often utilizes time resolved reactions that target different states or parameters thought to have the highest impact on detonation wave structure such as the CJ state or induction length. The more parameters that are matched, usually, the more difficult it is to implement and tune the model. Simple models usually rely on global reaction mechanisms which typically involve less than 10 reactions. One-step mechanisms that involve only carbon dioxide and water as products are often too far from realistic detonation conditions, so, the product species are manipulated to give desirable end states. The use of a full chemical mechanism, such as JetSurF2.0 [3], in combination with software such as Cantera [1] and the SD Toolbox [2] can offer a prediction on what the end thermodynamic state and flow structure would be for an ideal, one-dimensional detonation. With the realistic end state in mind, a new mechanism can be derived of the form $Reactants \rightarrow Products$ where the products are a linear combination of the most abundant species in the realistic CJ state. This does a good job of reproducing the desired CJ state, but requires additional tuning to determine the conversion rate of reactants to products that will first give a detonation, then reevaluation for the path in between.

2.3.1 Induction Parameter Model

Induction parameter models have many different forms, but tend to accomplish the same thing in the end [72]. IPM models are usually 1-step, global mechanisms that postpone chemical reactions through the use of a curve fit ignition delay time (IDT) then convert species and add the energy associated with the reaction through the use of source terms. IPM models have one huge benefit which manifests in the form of easy implementation and low computational cost. This sim-

plicity becomes somewhat of a burden when it comes to often heuristic analysis of such models. Ignition delay times are often commonly available for hydrocarbon fuels, and are even sometimes generalized for a set of fuels such as this relation for n-alkanes from [73] at an equivalence ratio of one,

$$t_{id} = 9.40 \times 10^{-6} \cdot P_{atm}^{-0.55} \cdot X_{O_2}^{-0.63} \cdot C^{-0.50} \cdot \exp\left(46,550/\mathcal{R}_c T\right) \tag{2.12}$$

where t is in microseconds and C is the number of carbon atoms in the fuel molecule. Once a time delay has been chosen, the product species should be calibrated to the realistic CJ state for the targeted equivalence ratio, such as what can be seen in Table 2.1. What becomes important here is the averaged molecular weight and adiabatic index of the product species. Once these are known, the appropriate 2-gamma heat release can be calculated according to Equation 2.13, where subscripts 1 and 2 refer to pre-shock and CJ state conditions, respectively.

$$\frac{q}{a_1^2} = \frac{\gamma_2 + 1}{2(\gamma_2 - 1)} \left(\frac{a_{CJ}}{a_1}\right)^2 - \left(\frac{1}{\gamma_1 - 1} + \frac{M_{CJ}^2}{2}\right) \tag{2.13}$$

Here, a is the speed of sound. All of the quantities seen in Equation 2.13 should be available or easily calculated from a CJ equilibrium state prediction, full derivation available in [2].

Probably the biggest challenge associated with the IPM model is how to choose an appropriate rate for the progression of the reaction. The previous implementation in FLASH [74] utilized a simple numerical stability approach that limited the maximum increase in internal energy by some percentage at the current time step. Once the allowable amount of energy increase was calculated (capped by reaction completion), the appropriate species conversion was done for reactants and products. Bulk detonation properties such as propagation velocity CJ state can be met with very low error, but there are some unintended consequences of the method. Reactions do not begin until a progress variable tracking the accumulated ignition delay time has reached a non-dimensional value of one. This progress variable is advected though the gas phase flow field (see Equation

2.14), somewhat nonphysically, but out of necessity to track where reactions can and cannot occur.

$$\frac{\partial \rho_g \tau}{\partial t} + \nabla \cdot \rho_g \tau \mathbf{v}_g = \frac{\rho_g}{t_{ind}} \tag{2.14}$$

The progress variable can be limited at a value of one to reduce the potential overreach it may have in neighboring computational cells, but numerical diffusion still smears the value. The effect this has is often the inappropriate guarantee of a reaction as long as a reaction occurred somewhere in the neighboring domain. While not necessarily running under an infinitely fast kinetics assumption, once a reaction has started, there is no stop or physically informed rate. The other disadvantage that tends to be a consequence of an arbitrary numerical stability limit on reaction progression is the size of the reaction zone. The size of the reaction zone in computational space has a large impact on detonation properties not as well quantified by the model up to this point, the prime example being detonation cell size. Without a well defined reaction time or length scale, the cell size can be anything the modeler chooses it to be so long as the stability limit they choose produces a detonation in the simulation.

Product Species	MW $[g_i/mol]$	X_i	Y_i
CO	28.0104	0.237082	0.286602
CO_2	44.0098	0.127660	0.242473
H	1.00794	0.048632	0.002116
H_2	2.01588	0.054711	0.004760
H_2O	18.01528	0.252280	0.196148
O	15.9994	0.051672	0.035679
OH	17.00734	0.127660	0.093702
O_2	31.9988	0.100304	0.138520

Table 2.1: CJ state product composition for n-Dodecane-O_2 detonation, $\phi = 1$.

2.3.2 Arrhenius Rate Kinetics

To resolve chemical reactions more accurately in time, a system of ordinary differential equations can be set up for a fixed number of reacting species (n_s, indexing below with i, j) involved

in a set amount of chemical reactions (n_r, indexing below with k). Following the methodology in [75], a general framework can be built for CFD codes which considers each finite volume computational cell as a constant internal energy and volume (UV) reactor. This system of equations is then integrated over the source term time step utilized in the operator splitting method. Reactions can be generally written as,

$$\sum_{i=1}^{n_s} \nu'_{k,i}(\text{Species})_i \longleftrightarrow \sum_{i=1}^{n_s} \nu''_{k,i}(\text{Species})_i \tag{2.15}$$

Reaction rate progress variables are often expressed by the law of mass action,

$$q_k(Y,T) = \kappa_{f,k} \prod_{i=1}^{n_s} \left(\frac{\rho Y_i}{MW_i}\right)^{\nu'_{k,i}} - \kappa_{b,k} \prod_{i=1}^{n_s} \left(\frac{\rho Y_i}{MW_i}\right)^{\nu''_{k,i}} \tag{2.16}$$

For the Arrhenius kinetic law, the forward and backward rates follow,

$$\begin{aligned}
\kappa_{f,k}(T) &= A_k \exp(-\frac{E_{a,k}}{\mathcal{R}_c T}) \\
\kappa_{b,k}(T) &= \kappa_{f,k}/K_{c_{eq},k} \\
K_{c_{eq},k}(T) &= \exp(-\Delta g_k^0) \left(\frac{P_{atm}}{\mathcal{R}T}\right)^{\sum_{i=1}^{n_s} \nu_{k,i}} \\
\Delta g_k^0 &= \sum_{i=1}^{n_s} \nu_{k,i} g_i^0 \\
g_i^0 &= H_i^0/(\mathcal{R}T) - S_i^0/\mathcal{R}
\end{aligned} \tag{2.17}$$

The system can now be expressed as a set of mass conservation equations for each reacting species,

$$\frac{dY_i}{dt} = \frac{MW_i}{\rho} \sum_{k=1}^{n_r} \nu_{k,i} q_k(Y,T), \quad i = 1, ..., n_s \tag{2.18}$$

System closure is obtained through conservation of energy,

$$\frac{dT}{dt}(Y,T) = \frac{-1}{\overline{C}_v(Y,T)} \sum_{i=1}^{n_s} \left(u_i \frac{dY_i}{dt}\right) \tag{2.19}$$

Altogether, this yields an initial value problem for a system of n_s+1 equations for n_s+1 unknowns,

$$\dot{\boldsymbol{y}} = \boldsymbol{f}(\boldsymbol{y}) = \begin{bmatrix} \dot{T} \\ \dot{Y}_1 \\ \vdots \\ \dot{Y}_{n_s} \end{bmatrix} \tag{2.20}$$

This system can potentially be reduced by one equation through exploitation of $\sum_{i=1}^{n_s} Y_i = 1$. The explicit formulation for the numerical solution comes naturally,

$$\begin{aligned} \boldsymbol{y}^{t+1} &= \boldsymbol{y}^t + \Delta t \boldsymbol{f}^t \\ \boldsymbol{y}^t &= \begin{bmatrix} T \\ Y_1 \\ \vdots \\ Y_{n_s} \end{bmatrix}^t \end{aligned} \tag{2.21}$$

While convenient, explicit solutions for chemically reacting systems are notorious for giving erroneous results and requiring very small time steps to prevent over-consumption of species. Implicit formulations are more commonly seen implemented, but require more work for problem formulation. As explained in [76], the formulation for the first order (semi-)implicit method can be expressed as,

$$\begin{aligned} \boldsymbol{y}^{t+1} &= \boldsymbol{y}^t + \Delta \boldsymbol{y} \\ (\tilde{\mathbf{1}}/\Delta t - \boldsymbol{J})\Delta \boldsymbol{y} &= \boldsymbol{f}^t \end{aligned} \tag{2.22}$$

This method has the same order of accuracy as the explicit method, however, the unconditional stability is often worth the matrix inversion involved. To increase the accuracy of the method over a computational time step, [76] recommends the use of a variable-order Bader-Deuflhard method, which has the potential to increase the accuracy of the method to order 15 at low programming

effort, but at additional computational cost as more matrix inversions are necessary. The formulation of the Jacobian matrix, $\boldsymbol{J}$, and the inversion of $(\tilde{\mathbf{1}}/\Delta t - \boldsymbol{J})$ are some of the biggest obstacles of implicit methods for chemical reactions. The implementations shown in this work utilize the first order implicit method with direct matrix inversion methods since the systems are small. The Jacobian matrix has the structure seen in Figure 2.1. Each component can be assembled as follows,

$$\begin{aligned}
J_{i+1,j+1} &= \frac{\partial}{\partial Y_j}\frac{dY_i}{dt} = \frac{MW_i}{\rho}\sum_{k=1}^{n_r}\left(\nu_{k,i}\frac{\partial q_k}{\partial Y_j}\right) \\
J_{1,j+1} &= \frac{\partial}{\partial Y_j}\left(\frac{dT}{dt}\right) = \frac{-1}{\overline{C}_v}\left[C_{v,j}\frac{dT}{dt} + \sum_{i=1}^{n_s} u_i \frac{\partial}{\partial Y_j}\left(\frac{dY_i}{dt}\right)\right] \\
J_{i+1,1} &= \frac{\partial}{\partial T}\left(\frac{dY_i}{dt}\right) = \frac{MW_i}{\rho}\sum_{k=1}^{n_r}\nu_{k,i}\frac{\partial q_k}{\partial T} \\
J_{1,1} &= \frac{\partial}{\partial T}\left(\frac{dT}{dt}\right) = \frac{-1}{\overline{C}_v}\left\{\frac{dT}{dt}\frac{\partial \overline{C}_v}{\partial T} + \sum_{i=1}^{n_s}\left[C_{v,i}\frac{dY_i}{dt} + u_i J_{i+1,1}\right]\right\}
\end{aligned} \tag{2.23}$$

The formulation described here has a much stronger physical background in comparison with the IPM formulation and allows for more precise quantification of reaction rates and there impact on the system. Considering the same one-step global system used in the IPM reaction, a common modification to the above formulation for an irreversible combustion reaction is to provide a rate of the form $q = A\exp(-\frac{E_a}{\mathcal{R}_c T})[Fuel]^a[O_2]^b$, where a and b are often chosen so the sum $a+b$ is equal to some constant. The sum $a+b$ will significantly effect the reaction rate and the constant targeted is usually dependent on the context of what physical application is being modeled. For instance, [77] choose the constant to be 1.75 to accurately capture the dependence of laminar flame speed on pressure.

One particular procedure for tuning global mechanisms, and the same used in the work to follow, is to choose a desired sum of $a+b$. Once $a+b$ has been chosen, the activation energy can be chosen such that the effective activation energy, θ, matches that of a detailed chemical kinetic mechanism. The method of calculation is detailed in [78]. Then, the pre-exponential factor is chosen to match critical ZND profile features, such as the induction length or exothermic pulse

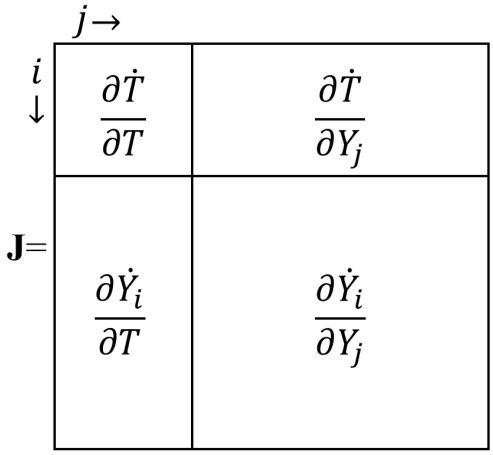

Figure 2.1: Jacobian matrix structure for the constant internal energy and volume formulation.

width. This is an iterative process and may require choosing several different values of a and b to match the features of greatest importance. This is generally done for one particular equivalence ratio but correction functions can be added to the rate to modify the pre-exponential factor for better performance across a wide range of conditions.

From [17], a global one-step reaction mechanism was chosen for n-dodecane-oxygen combustion for $\phi = 1$ of the form $q = 6.6E13 \exp(-\frac{46{,}500}{\mathcal{R}_c T})[Fuel]^{0.75}[O_2]$, and will be used for the n-dodecane-oxygen detonations presented later.

2.3.3 n-Dodecane-Air Modeling

Future simulations will likely need the capabilities to model air combustion. While a more chemically isolated system from nitrogen, pure oxygen combustion is not practical for most air breathing engines. Pure oxygen combustion was chosen as an experimental approach in [31] for a few key reasons. Detonation cell widths are much smaller when diluents, e.g., nitrogen or argon, are not present in the experiment. This allows for a smaller tube diameter with stably propagating detonations. This also allows for more extreme conditions to observe. While interesting as a fundamental research problem, pure oxygen combustion is accompanied by many challenges. When modeling pure oxygen combustion, properties such as adiabatic flame temperature or CJ speed become extremely sensitive to product composition, meaning simple models that only consider

products to be CO/CO_2 and H_2O cannot adequately reproduce physical conditions such as end state temperatures differing by over a thousand Kelvin from realistic conditions. This means that either product needs to be calibrated to realistic equilibrium conditions or the reaction mechanism needs to incorporate more species (and generally more reactions). Using a mechanism similar to what is proposed by [79], which includes 9 reactive species, very low errors can be obtained for both air and oxygen combustion. Consider the following general hydrocarbon reactions,

$$C_nH_m + (n + \frac{m}{4})O_2 \longrightarrow nCO_2 + \frac{m}{2}H_2O \tag{2.24}$$

$$\begin{aligned} C_nH_m + (\frac{n}{2} + \frac{m}{4})O_2 &\longrightarrow nCO + \frac{m}{2}H_2O \\ CO + \frac{1}{2}O_2 &\longleftrightarrow CO_2 \end{aligned} \tag{2.25}$$

$$\begin{aligned} C_nH_{2m} + \frac{n}{2}O_2 &\longrightarrow nCO + mH_2 \\ CO + O &\longleftrightarrow CO_2 + M \\ CO + OH &\longleftrightarrow CO_2 + H \\ H_2 + O_2 &\longleftrightarrow OH + OH \\ H + O_2 &\longleftrightarrow OH + O \\ OH + H_2 &\longleftrightarrow H_2O + H \\ O + H_2 &\longleftrightarrow OH + H \\ OH + OH &\longleftrightarrow H_2O + O \\ H + H &\longleftrightarrow H_2 + M \\ H + OH &\longleftrightarrow H_2O + M \end{aligned} \tag{2.26}$$

It can be seen in Table 2.2 that as the complexity of the mechanism increases, the better the results are in comparison with detailed mechanisms. Further complicating matters with oxygen detonations are the physical length scales involved in the ZND structure. From Cantera [1] with the SD Toolbox [2] using the JetSurF2.0 detailed chemical mechanism [3], the induction length

and exothermic pulse width are estimated to be 26.8 and 6.5 μm, respectively, for an equivalence ratio of one. This becomes extremely difficult to adequately resolve in full scale 2D and 3D CFD simulations. Considering other physical length scales at play in multiphase detonations, like droplet diameters, it becomes impossible to resolve both length scales with most common modeling methods. In [17], the minimum grid size used was nearly 10 times larger than the induction length of an oxygen detonation out of necessity to include droplets of believable sizes that could be produced by nozzles. Using the same predictive methods as above, it can be estimated that the scales involved in a stoichiometric n-dodecane-air detonation would be 1364 and 145.4 μm for the induction length and exothermic pulse width. The feasibility of successfully resolving both the detonation length scales and the droplet length scales increases under these conditions.

Mechanism	$D_{CJ} \times 10^{-2}$ [cm/s]	T_{CJ} [K]	P_{CJ} [atm]	$T_{ad,UV}$ [K]	$T_{ad,HP}$ [K]
Eqn. 2.24	1907.6	3240.7	20.3	2929.2	2412.1
Eqn. 2.25	1826.8	2938.6	19.1	2714.8	2309.6
Eqn. 2.26	1803.1	2855.8	18.8	2658.9	2283.9
JetSurF2.0 [3]	1802.5	2853.7	18.8	2657.1	2282.4

Table 2.2: CJ Detonation conditions and T_{ad} from UV and HP flame calculations for $C_{12}H_{26} + 18.5(O_2 + 3.76N_2)$ combustion from initial state T = 298.15 $[K]$ and P = 1 $[atm]$ (stoichiometric mixture, $\phi = 1$). Generated with both Cantera [1] and the SD Toolbox [2].

2.3.3.1 One-Step Global Mechanism

Similar to what was implemented in [17], a single-step global mechanism was tuned for air detonations considering an equivalence ratio of one and air having the composition $O_2 + 3.76N_2$. The rate is of the form,

$$q = 8.5E8 \exp(-\frac{40,750}{\mathcal{R}_c T})[Fuel]^{0.05}[O_2]^{0.95} \tag{2.27}$$

and having a specified product composition as seen in Table 2.3. This mechanism is capable of matching the ZND profile very closely while also having a similar effective activation energy as

seen in Figure 2.2 and Table 2.4.

Product Species	MW [g/mol]	X_i	Y_i
CO	28.0104	0.071564	0.113472
CO_2	44.0098	0.130659	0.325511
H	1.00794	0.109230	0.006232
HO_2	33.00674	0.000020	0.000037
H_2	2.01588	0.185943	0.021219
H_2O	18.01528	0.422763	0.431141
O	15.9994	0.007533	0.006823
OH	17.00734	0.041688	0.040135
O_2	31.9988	0.030600	0.055429

Table 2.3: CJ state product composition for n-Dodecane-$18.5(O_2 + 3.76N_2)$ detonation predicted by JetSurF2.0 [3], T=298.15 $[K]$, P=1 $[atm]$, $\phi = 1$.

This implementation used in multiphase detonation modeling will likely produce results similar to what were seen in [17], with one of the drawbacks of such a mechanism being that it was tuned for one particular initial state and equivalence ratio. This is currently seen as a limitation as one of the key findings in [17] was how multiphase detonations are different from premixed gaseous detonations because of the nonuniform equivalence ratio distributions throughout the flow field.

Property	JetSurF2.0 [3]	Single Step
$D_{CJ} \times 10^{-2}$ $[cm/s]$	1802.5	1801.4
P_{CJ} $[atm]$	18.8	18.1
T_{CJ} $[K]$	2853.7	2832.4
Δx_{ind} $[cm]$	0.1364	0.1345
Δx_{exo} $[cm]$	0.01454	0.02673
θ	10.66	10.60

Table 2.4: CJ and ZND Parameters for global 1-step mechanism.

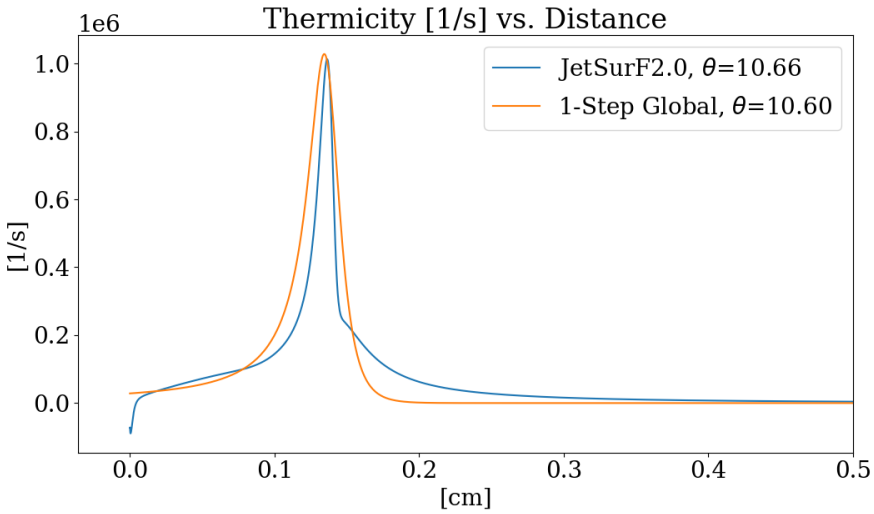

Figure 2.2: Thermicity vs. distance for n-dodecane-air detonation. Comparison between a detailed [3] and a global 1-step mechanism.

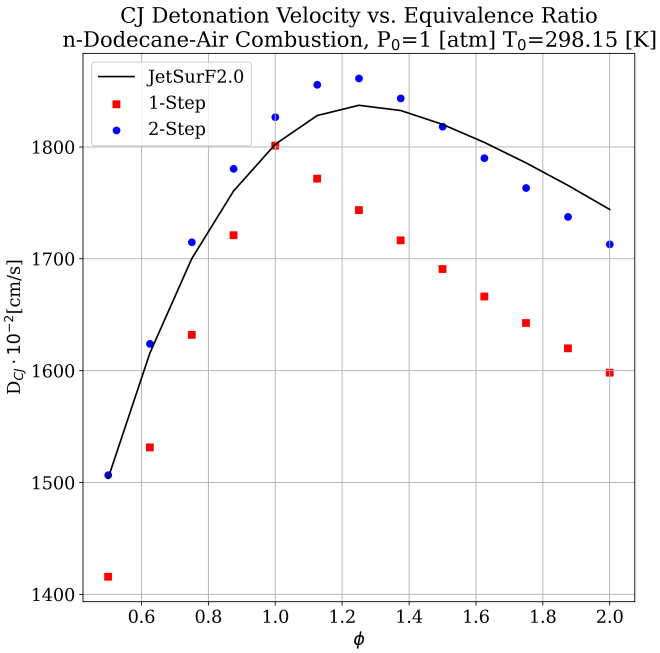

Figure 2.3: CJ detonation speed vs. equivalence ratio for n-dodecane-air combustion. The mechanisms utilized for calculations are the detailed JetSurF2.0 [3], the tuned one-step mechanism from Section 2.3.3.1, and from the generalized two-step mechanism presented in Section 2.3.3.2.

2.3.3.2 *Two-Step Global Mechanism*

In an effort to expand the capabilities of the FLASH code, the mechanism seen in Equation 2.25 was implemented in a general form to allow for the use of two-step chemistry with an easily modifiable fuel consumption rate. Without meticulous tuning of one-step or product tuned mechanisms for different equivalence ratios, such as [80], they become nonviable for general use. This can be visualized in Figure 2.3, where the CJ detonation velocity has been compared for different product species compositions. Outside of the tuned conditions of an equivalence ratio of one, the mechanism proposed in Section 2.3.3.1 performs rather poorly in comparison with mechanisms that allow for variations in product composition. Despite the simplicity of the global two-step mechanism, it removes the necessity for product composition tuning while giving reasonable detonation speeds compared to detailed chemistry. Thus, the focus of the mechanism now shifts to kinetics. Works such as [77] provide general guidance into how rates should be chosen for simplified, two-step mechanisms while more modern works, such as [81], give more explicit methodology and formulations for two-step combustion modeling.

The test case chosen for initial implementation was the B. Franzelli-E. Riber (BFER) kerosene mechanism [82]. This mechanism was chosen because it was tuned for a wide range of equivalence ratios and capable of giving reasonable results for low speed combustion. When applying the same mechanism to detonations, the mechanism still gives results that are reasonable (see Table 2.5 for relevant length scales). The mechanism was implemented composing of the following reaction rates,

$$\begin{aligned} q_1 &= A_1 f_1(\phi) \exp(\frac{E_{a,1}}{\mathcal{R}_c T})[C_n H_m]^a [O_2]^b \\ \kappa_{f,2} &= 4.5E10 f_2(\phi) \exp(\frac{20,000}{\mathcal{R}_c T}) \\ q_2 &= \kappa_{f,2}[CO][O_2]^{0.5} - \kappa_{b,2}[CO_2] \end{aligned} \tag{2.28}$$

where the backward reaction rate is computed from the identity in Equation 2.17. Constants a, b, A_1, and $E_{a,1}$ are provided in [82] for kerosene. The functions f_k in Equation 2.28 are correction

functions for equivalence ratio of the forms,

$$
\begin{aligned}
f_1 =& \frac{2}{\left[1+\tanh\left(\frac{\phi_{01}-\phi}{\sigma_{01}}\right)\right] + B_1\left[1+\tanh\left(\frac{\phi-\phi_{11}}{\sigma_{11}}\right)\right] + C_1\left[1+\tanh\left(\frac{\phi-\phi_{21}}{\sigma_{21}}\right)\right]} \\
f_2 =& \frac{1}{2}\left[1+\tanh\left(\frac{\phi_{02}-\phi}{\sigma_{02}}\right)\right] + \frac{B_2}{2}\left[1+\tanh\left(\frac{\phi-\phi_{12}}{\sigma_{12}}\right)\right] + \\
& \frac{C_2}{2}\left[1+\tanh\left(\frac{\phi-\phi_{22}}{\sigma_{22}}\right)\right]\cdot\left[1+\tanh\left(\frac{\phi-\phi_{32}}{\sigma_{32}}\right)\right]
\end{aligned}
\tag{2.29}
$$

where in the current implementation the above constants σ_{ij} and ϕ_{ij} are the same as what is provided in [82]. A zero-dimensional constant internal energy and volume reactor was programmed to verify the implicit formulation of the system, the results of which can be seen in Figure 2.4.

Once the implementation was verified, the framework was imported into FLASH and run with n-dodecane instead of kerosene. The gaseous conditions presented here are at the boiling point of n-dodecane (490 $[K]$). The ZND structure for the mechanism is still reasonable compared to the full mechanism, and a full comparison can be seen in Table 2.5 for an equivalence ratio of one. The pressure profile obtained in the 1D FLASH simulations along with the species mass fractions near the von Neumann spike can be seen in Figure 2.5. The minimum grid resolution used in 1D was 312.5 μm, which was due to oscillations in the solution that became too strong at finer resolutions and either gave erroneous data or decoupled the reaction and shock fronts. An example of such oscillations can be seen in the von Neumann spike over time (Figure 2.6). Monitoring the fluctuations in von Neumann spike pressure over time can also provide insight into when the numerical detonation has reached a stable propagation speed.

Property	JetSurF2.0 [3] (Cantera)	Two-Step (Cantera)	Two-Step (FLASH)
$D_{CJ} \times 10^{-2}\ [cm/s]$	1789.7	1821.5	1843.7
$P_{CJ}\ [atm]$	11.5	11.8	11.7
$T_{CJ}\ [K]$	2888.0	2999.0	3067.7
$\Delta x_{ind}\ [cm]$	0.09981	0.04432	–
$\Delta x_{exo}\ [cm]$	0.01798	0.02500	–

Table 2.5: Detonation parameters for the detailed and the global 2-step mechanisms from Cantera and the results obtained from FLASH for the global mechanism. T_0=490 $[K]$, P_0=1 $[atm]$, ϕ=1.

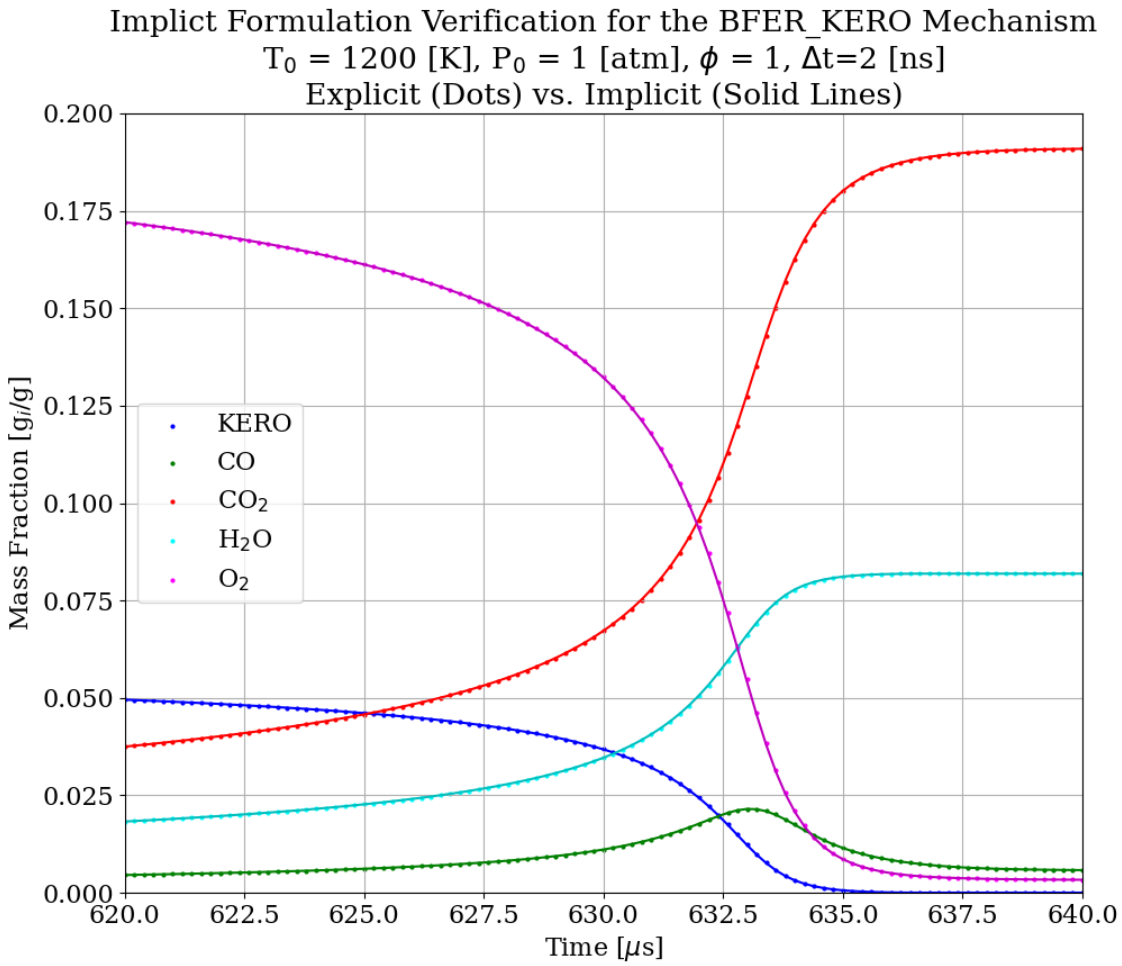

Figure 2.4: Mass fractions vs. time for both explicit and implicit formulations of the BFER kerosene system.

2.4 Droplet Heat and Mass Transfer Coupling

Transient modeling of heat and mass transfer can be sensitive to the material properties evaluated at each time step if there are large differences in the initial conditions of one state and the free stream. The inclusion of temperature and/or pressure dependent properties allows for greater confidence in the results obtained from reduced order models. For droplets initially at 298.15 $[K]$ entering free stream conditions potentially greater than 4000 $[K]$ and pressures well above the critical point, variations in properties cannot be neglected. The models and results in the following sections utilize the same approach taken in [17] for material property evaluation of liquid and vapor n-dodecane and gaseous oxygen. Saturated pressure, viscosity, surface tension, specific heat, enthalpy, latent heat, and thermal conductivity are assumed to be purely functions of temperature while liquid density and the binary diffusion coefficient are assumed to be both functions of temperature and pressure. A detailed list of material properties is provided in the same reference work. For a generic property A evaluated at the film conditions, the relation $\bar{A} = A_s + A_r(A_\infty - A_s)$ was used to interpolate between the surface and free stream conditions. The constant A_r was taken to be 1/3 for all properties evaluated. For thermodynamic consistency in the numeric implementation, the fuel liquid enthalpy was always found by the relation $h_l = h_g - h_{fg}$ where h_g is the gas enthalpy obtained from the NASA polynomial form and h_{fg} is the latent heat of vaporization curve fit from NIST data. It is important to note that throughout the lifetime of the liquid drop, it will reach the critical point under oxygen detonation conditions. Droplet temperature and evaluation of liquid properties is capped at this point. Although the film temperature is still able to change, the impact observed on vaporization is a nearly constant mass loss rate at this point.

2.4.1 Droplet Breakup

The droplet breakup mechanism utilized in this work is referred to as (the) WERT49 (model) because it is a modification of Wert's [49] original model for droplet breakup at low Mach number. Wert utilized shock tube data and then the model was re-tuned by [52] for newer shock tube data. This model is empirical and, as somewhat expected, it gives fairly good estimates for droplet

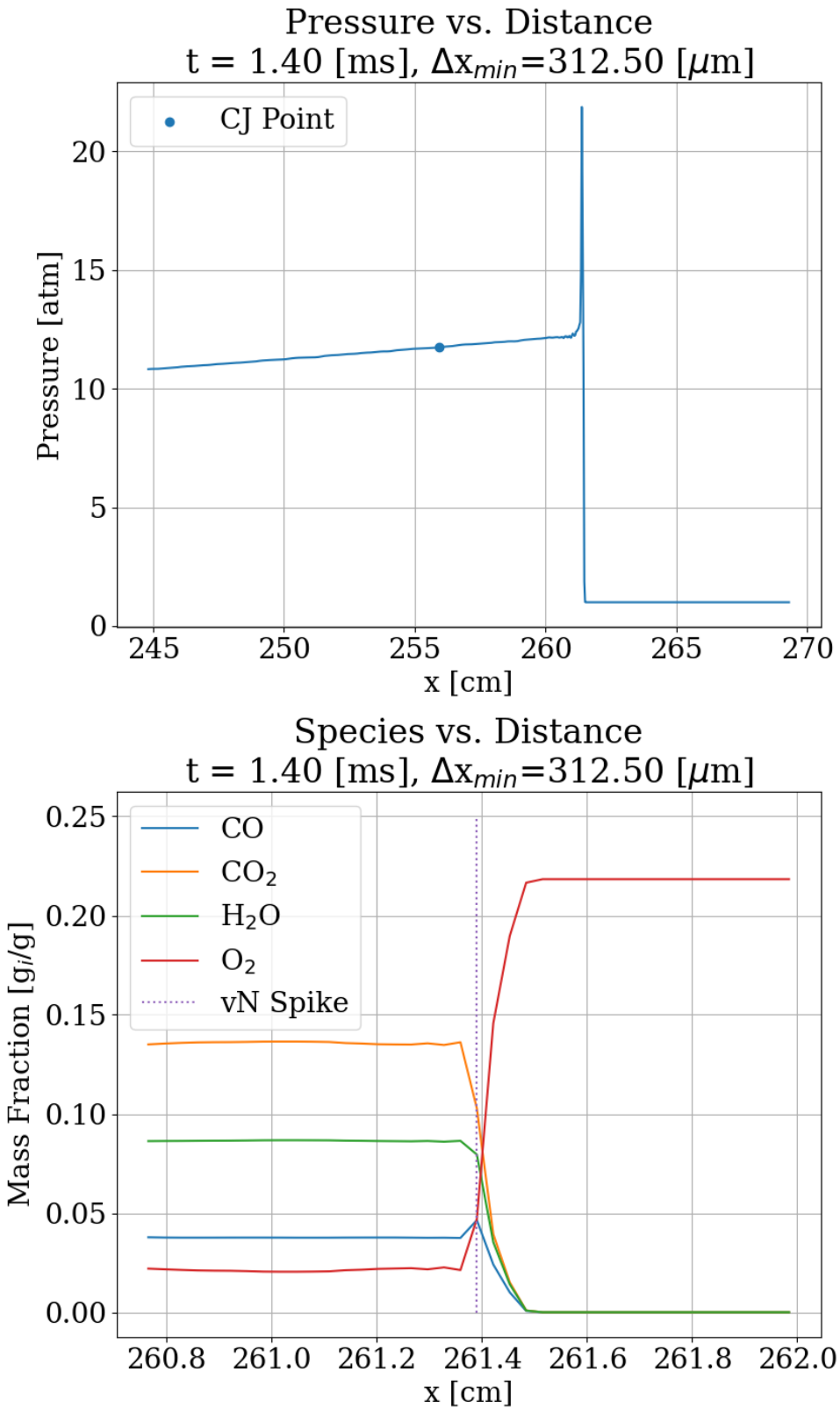

Figure 2.5: Pressure profile from a late simulation time step (top) and species mass fractions profiles near the von Neumann spike (bottom). Results from FLASH.

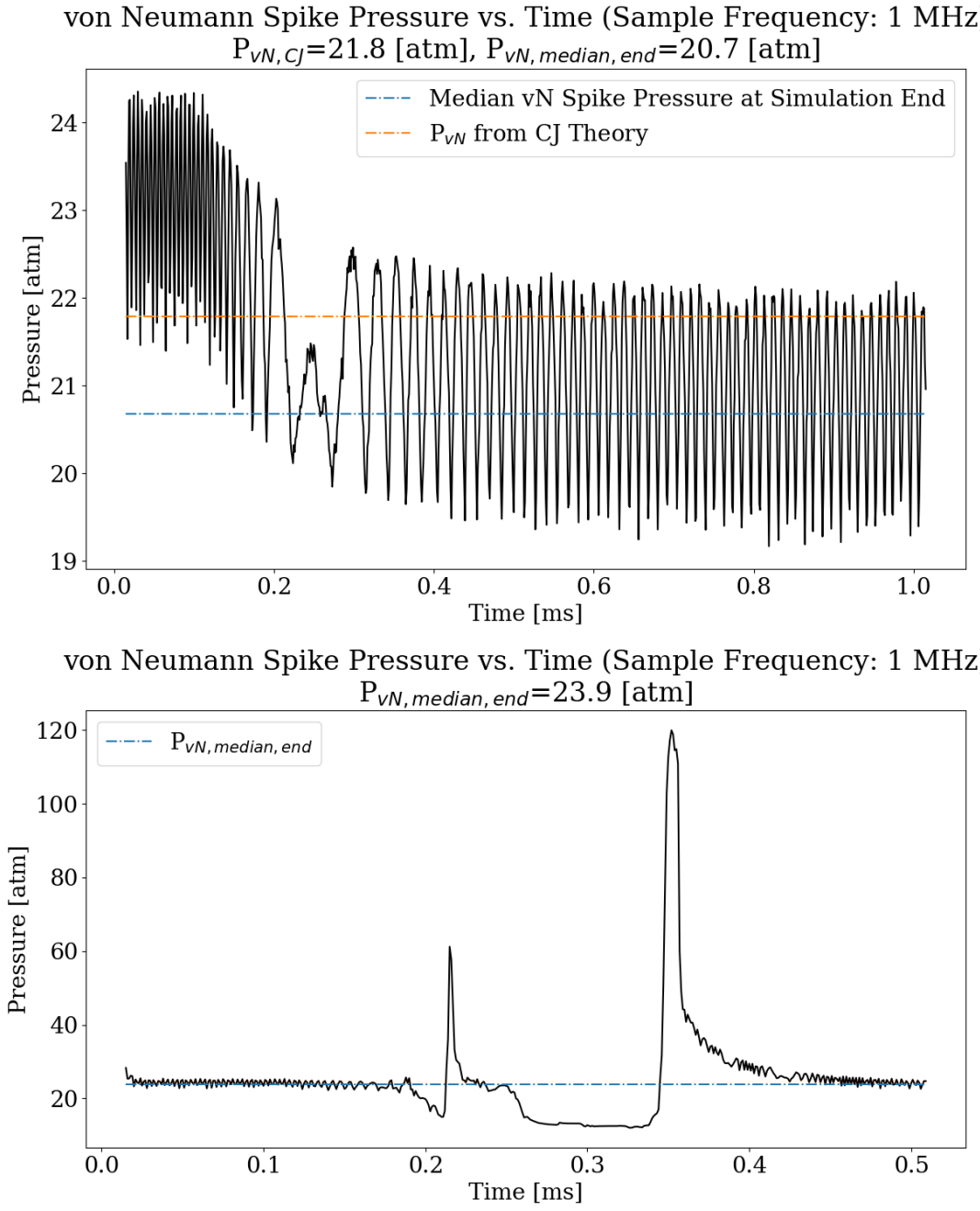

Figure 2.6: A sampling of the von Neumann spike pressure over time (FLASH). (Top) $\Delta x_{min} = 312.50\ [\mu m]$ (Bottom) $\Delta x_{min} = 156.25\ [\mu m]$. As the detonation becomes more steady, the median value of the fluctuations tends toward a constant value. If the level of refinement is too high, numerical oscillations result in unstable behavior.

lifetimes in post shock conditions for the conditions under which it was developed [53]. Minor modifications have been made depending on the application [52, 53, 17] but the methodology utilized in this work is detailed in [17]. A schematic of the numerical breakup process can be seen in Figure 2.7.

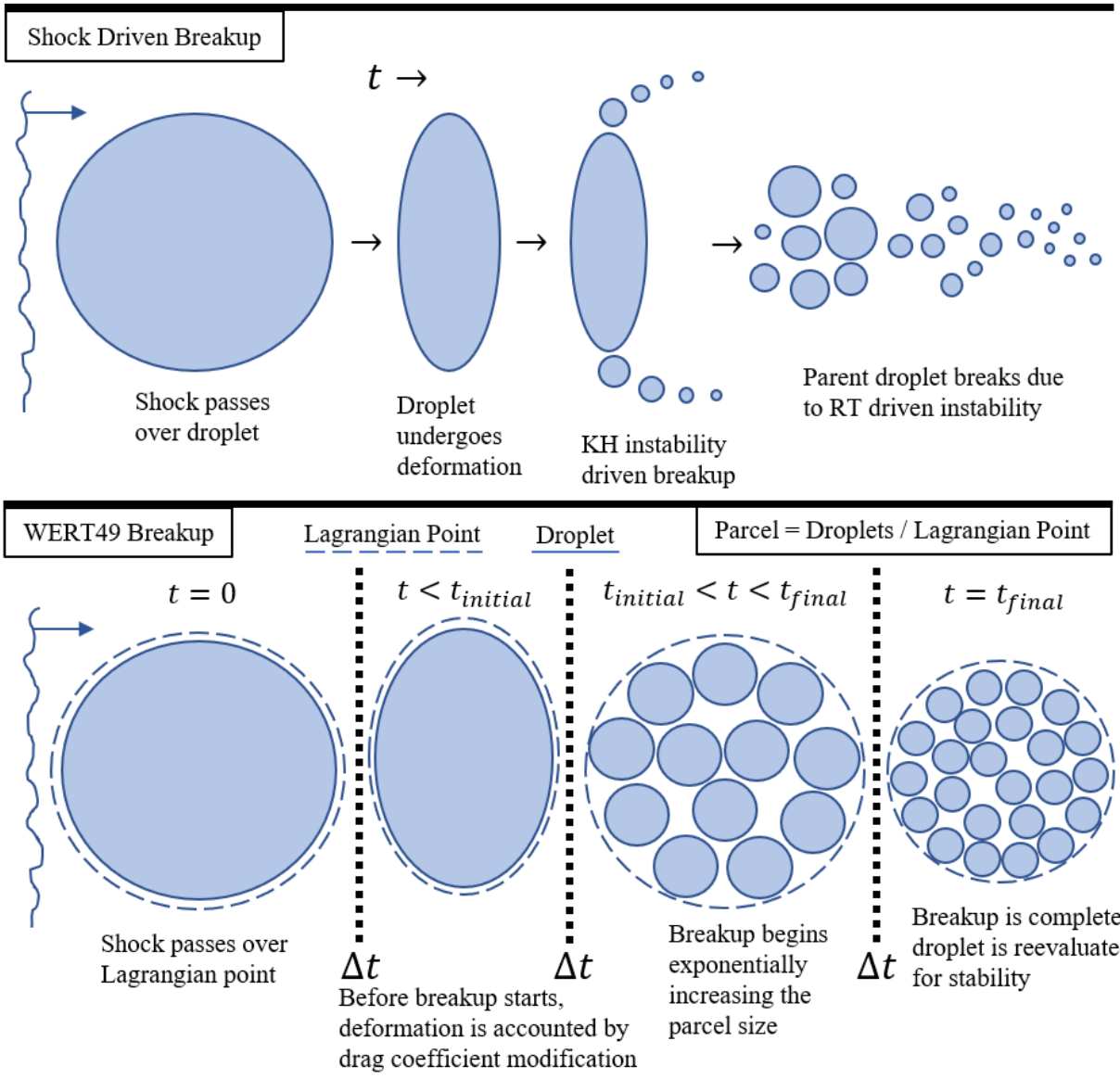

Figure 2.7: Progression of breakup over time from a physical and modeling perspective (WERT49).

2.4.2 Droplet Vaporization

Reduced order droplet vaporization models often take similar forms but with different exact formulations attempting to predict or correct for realistic physical behavior. Most zero-order models provide a formulation for $\dot{m}$ which can then be appropriately discretized in time to provide a vapor source term. Once the mass transfer is known heat transfer into the droplet can be computed as,

$$\begin{aligned} mC_{p,l}\dot{T} &= \dot{Q} + \dot{m}h_{fg}(T_s) \\ \dot{Q} &= \pi d_p \overline{\lambda}_g Nu\,(T_\infty - T_s) \end{aligned} \tag{2.30}$$

where the Nusselt number is dependent on the model/correlation chosen.

2.4.2.1 Abramzon-Sirignano (A-S)

The Abramzon-Sirignano formulation [48] is widely used and provides reasonable results for vaporization under a wide range of convective free stream conditions. Early models [60, 83] often came from assumptions of low convective forces and a unity Lewis number, yielding formulations that give Spalding mass transfer numbers, B, that are assumed equal to each other. The A-S formulation attempts to correct this assumption through a series of relations that quantify the magnitude of conductive and convective forces for a given moment in time and provides different Spalding transfer numbers for both mass (B_M) and heat (B_T) transfer. The model is as follows,

$$\begin{aligned} \dot{m} &= \pi d_p \overline{\rho}\mathcal{D}ShB_M \\ B_M &= \frac{Y_{F,s} - Y_{F,\infty}}{1 - Y_{F,s}} \\ Sh &= Sh^* \frac{1 + B_M}{B_M} \\ Sh^* &= 2 + (Sh_0 - 2)/F_M \end{aligned} \tag{2.31}$$

where Sh_0 can be an explicit evaluation or a generalized correlation for Sherwood number. The film correction function F is expressed as $F(B) = (1+B)^{0.7\frac{\ln(1+B)}{B}}$, being purely a function of

the associated transfer number. Heat transfer then becomes reliant on the Nusselt number which is obtained from an iterative approach,

$$\begin{aligned} Nu &= Nu^* \frac{1+B_T}{B_T} \\ Nu^* &= 2 + (Nu_0 - 2)/F_T \\ B_T &= \frac{\overline{C}_{pF} \cdot (T_\infty - T_s)}{h_{fg}(T_s) + \dot{Q}/\dot{m}} = (1+B_M)^\psi - 1 \\ \psi &= \left(\frac{C_{p,F}}{\overline{C}_{p,g}}\right)\left(\frac{Sh^*}{Nu^*}\right)\frac{1}{\overline{Le}} \end{aligned} \tag{2.32}$$

where Nu_0, like Sh_0, can be an explicit evaluation or a generalized correlation for Nusselt number. For all models considered in this work, the formulations from [84] are used for Nusselt and Sherwood number calculation as seen in Equation 2.33.

$$\begin{aligned} Sh_0 &= 1 + (1 + Re\overline{Sc})^{1/3} f(Re) \\ Nu_0 &= 1 + (1 + Re\overline{Pr})^{1/3} f(Re) \\ f(Re) &= \begin{cases} 1 & Re \leq 1 \\ Re^{0.077} & Re > 1 \end{cases} \end{aligned} \tag{2.33}$$

One last important specification is that the Reynolds number is evaluated with mixed properties using a weighted viscosity for the film conditions, $Re = \frac{\rho_\infty |\boldsymbol{u_\infty} - \boldsymbol{u_p}| d_p}{\overline{\mu}_g}$

2.4.2.2 Combustion Effects

The effects of a combusting droplet can be incorporated into the formulation of $\dot{m}$ mainly through modification of the transfer number. Adapted from [47], the incorporation of a combustion mass transfer number, B_C, is expressed as

$$\begin{aligned} \dot{m} &= \pi d_p \overline{\rho} \mathcal{D} Sh_0 \ln(1 + B_C) \\ B_C &= \frac{\overline{C}_{pF} \cdot (T_\infty - T_s) + LHV \cdot Y_{o,\infty}/\varsigma}{\dot{Q}/\dot{m} + h_{fg}(T_s)} \end{aligned} \tag{2.34}$$

where the term $\dot{Q}/\dot{m}$ is taken to be zero in this analysis for simplification since the latent heat of vaporization is orders of magnitude larger. Take note that if the value of $Y_{o,\infty}$ drops to zero, the value of B_C becomes equal to B_T from the A-S model.

2.4.2.3 A Combined Model (GORBEH)

Pure vaporization or combustion models often do not consider the presence of reactions or lack thereof and are often built for steady-state free stream conditions. Another important aspect to address is that convective conditions may blow the flame off of the droplet into the wake or completely prohibit burning. The transition of burning modes is reported to occur in a range of low relative Reynolds number ($Re_r \lesssim 200$) and can be seen experimentally in [61] and numerically in [63, 64]. There is no well defined model that specifies when this transition occurs, but there is both an analytical definition and empirical relation (tuned to simulation data) presented in [63]. A key takeaway from the work presented in [63] is that the hypothesis of the droplet multistate flame structure (envelope, wake, or boundary layer flames) is dependent not only on convective conditions but also free stream temperature and pressure. Another important aspect of the transition to wake burning is that the vaporization rate is then simply equal to that of the non-burning droplet conditions.

This work a proposes a new Global Order Reduced Burning Evaporation and Heating (GORBEH) model that allows for the combination of vaporization models informed on the free stream conditions a droplet is exposed to. The implementation in this work utilizes the A-S formulation for conditions above a relative Reynolds number criteria and under conditions where burning would not be possible without an ignition source. When the relative Reynolds number drops below the cutoff criteria, and ignition is possible (numerically detected by free stream temperature and oxygen content), the vaporization model switches to the combustion formulation detailed in section 2.4.2.2. From [61], the transition from envelope to wake burning is reported to occur around $Re_r \approx 138$, in [63] transition can be seen to occur as low as $Re_r \approx 50$, and [62] report a critical value around $Re_r \approx= 250$. The studies in [63, 62] both report trends of the critical transition occurring at higher Reynolds number values with increasing ambient conditions. An assumption

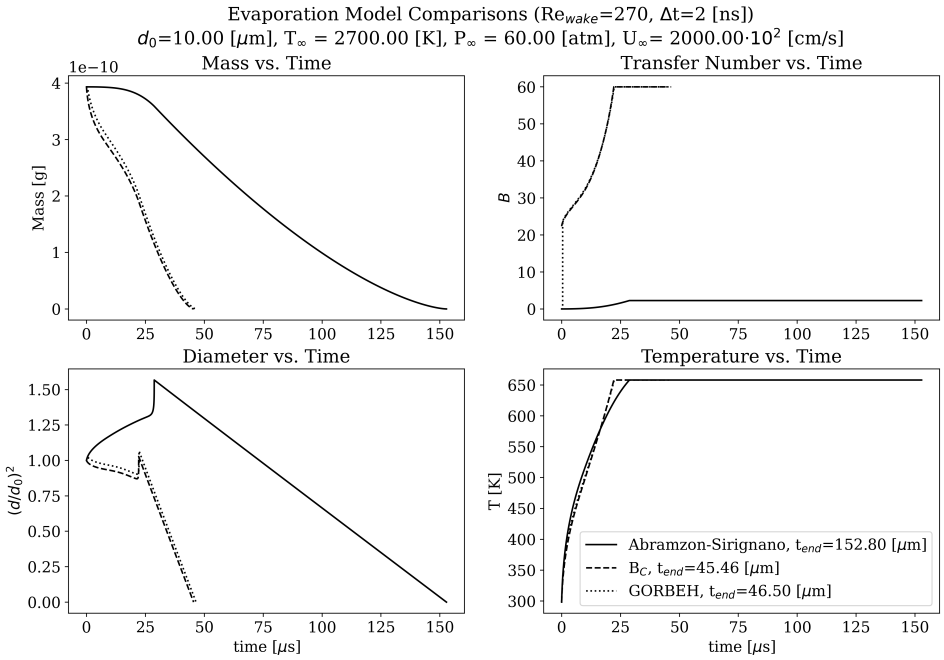

Figure 2.8: A comparison of the evaporation models presented under constant, detonation-like conditions.

made in this work is that the transition to wake burning or pure vaporization is at the end of the unsteady wake regime in laminar flow for a sphere [47], which is $Re_r = 270$. Without, a definitive value to pin down the regime, the reasoning for this choice reverts back to information from the well characterized system of flow past a sphere where the transition to turbulence is well documented. At a Reynolds number of 270, there is confidence that regular vortex shedding is occurring and flow past the sphere is now in the transition to turbulence. Below this criteria, oscillations in the flow field are long period and still characterized as laminar, meaning that flames may be able to gain stability and form in both envelope and boundary layer states. Additionally, the transition appears to take place at Reynolds numbers below this value, potentially in a wide range of $Re_r \approx 25 - 250$. The assumption made here has the potential to over-predict envelope burning modes in the current study, but this may actually help quantify how much this modification is able to impact the detonation wave propagation.

A comparison of the models described can be seen in Figure 2.8 where a zero-dimensional

method similar to [53] was taken for one-way coupling of particles to gas to numerically advance the solutions over time. The free stream was taken as constant for conditions similar to the detonation wave front. Under such conditions, the particle velocity equilibration time is relatively low, thus the GORBEH model largely follows the combustion model utilizing B_C for the majority of its life. The difference in droplet lifetime between the A-S and combustion model is on the order of 100 $[\mu s]$ for a 10 $[\mu m]$ droplet, $\approx 70\%$ faster when considering combustion. Both models predict supercritical droplet temperatures, the effects of which can most easily be seen in the subplot depicting non-dimensionalized diameter over time. The spike seen is a result of the density reaching its critical value, expanding the mass to a larger volume, and thus larger diameter.

2.5 CFD Simulation Initial Conditions

Numerical detonation initiation can be achieved through either a detonation-to-deflagration transition or a direct initiation from high temperature and pressure pockets initialized in the domain away from points of interest. The work presented here utilizes direct initiation methods. The multiphase detonation results start the simulation with four hot circular regions on the far left of the domain with develop into a steady gaseous detonation by the time it reaches the particle seeded region at 10 cm (see Figure 2.9). The purely gaseous detonation results utilized a singular curved hot spot on the far left of the domain to avoid influencing the cellular structure obtained. Multiphase simulations utilize initial ambient conditions of $T_0 = 298.15\ [K]$ and $P_0 = 1\ [atm]$ while the purely gaseous cases use the boiling point of n-dodecane, $T_0 = 490\ [K]$ at atmospheric pressure. All conditions are setup up for a global equivalence ratio of one, with gaseous conditions being completely premixed. All boundary conditions are set as reflecting/no-penetration to simulate shock tube conditions.

Droplet spatial distributions studied in previous works such as [37, 15, 17] utilize both uniform and normal distributions for droplets. Both have benefits to modeling but normal distributions are closer to physical conditions. The same applies for droplet diameters, uniform distributions can provide useful tools for isolating the effect of one particular diameter in simulations but a distribution of sizes is generally required for realistic spray conditions. Common distributions utilized to

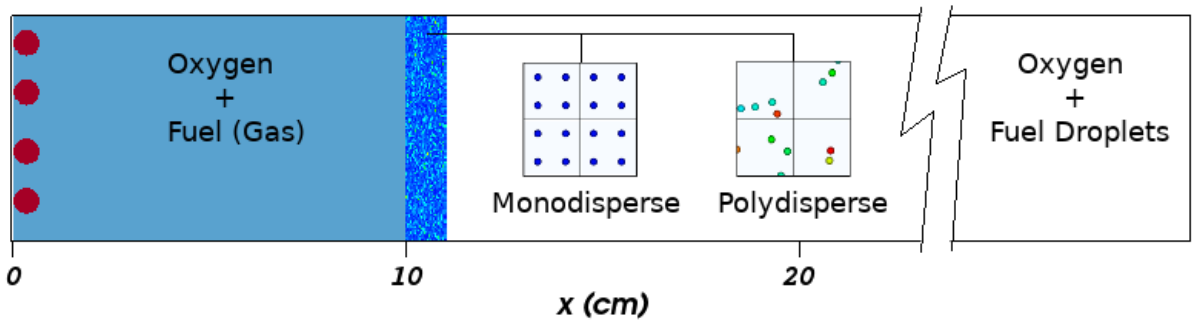

Figure 2.9: Computational domain setup for multiphase simulations. Reproduced with permission from [17].

represent droplet sprays are the lognormal and the Rosin-Rammler (Weibull) distribution. The the uniform distribution is utilized for droplet positions while the lognormal distribution is utilized for droplet sizes in this work with details of the lognormal distribution to follow in the next section.

2.5.1 The Lognormal Distribution for Droplet Sizes

Droplet sizes in sprays are commonly discussed in terms of statistical moments of the distribution given by the formula,

$$d_{ab} = \left[\frac{\sum N_i d_i^a}{\sum N_i d_i^b}\right]^{1/(a-b)} \tag{2.35}$$

where N is the number of droplets of that size in the distribution. There are key values of d_{ab} that are usually discussed in terms of specific applications [85], a handful can be seen in Table 2.6. Instruments like a Phase Doppler Particle Analyzer (PDPA), used for characterizing droplet spray distributions, often by default report the values of d_{10}, d_{20}, d_{30}, d_{32}, and d_{43}. Once the characteristic sizes of a spray are known, a lognormal distribution of mean μ and standard deviation σ can be fit to those sizes using Equations 2.36 and 2.37. Only two quantities are required from either Equation 2.36 or 2.37 to pin down the entire distribution.

$$\begin{aligned} \mu &= \ln(d_{50\%}) \\ \sigma &= \ln\left(\frac{d_{84.13\%}}{d_{50\%}}\right) = \ln\left(\frac{d_{50\%}}{d_{15.87\%}}\right) \end{aligned} \tag{2.36}$$

$$\begin{aligned}
\ln(d_{10}) &= \mu + 0.5\sigma^2 \\
\ln(d_{20}) &= \mu + 1.0\sigma^2 \\
\ln(d_{30}) &= \mu + 1.5\sigma^2 \\
\ln(d_{32}) &= \mu + 2.5\sigma^2 \\
\ln(d_{43}) &= \mu + 3.5\sigma^2
\end{aligned} \tag{2.37}$$

The distribution utilized in this work is the same as what was chosen in [17] for a $d_{10} = 10\ [\mu m]$ and $d_{32} = 18\ [\mu m]$ with a maximum diameter cutoff size of $d = 45\ [\mu m]$. This corresponds to $\mu = -7.747849$ & $\sigma = 0.542119$, and an initial constant parcel size of 63 yielding 4,022,249 total particles in the simulation for an equivalence ratio of one ($\phi = 1$).

Characteristic d_{ab}	Name	Application
d_{10}	Length, arithmetic	Comparisons, evaporation, comparison of disperse systems
d_{20}	Surface (area)	Surface area controlling, surface phenomena, e.g. absorption, vaporization
d_{21}	Surface Area-Length, Relative Surface	Absorption, adsorption, drop disintegration
d_{30}	Volume	Volume controlling, volumetric phenomenon, e.g. hydrology
d_{31}	Volume-Length, Relative Volume, Probert	Evaporation, molecular diffusion, combustion
d_{32}	Sauter (SMD), Volume-Surface	Mass and heat transfer, reaction, combustion, efficiency studies, drop range, dispersion
d_{43}	De Broukere, Herdan, Mass	Combustion equilibrium, drop fractionation

Table 2.6: Characteristic droplet diameters and some of their common applications.

3. RESULTS

The information presented in this section will highlight the effects of improved reactions modeling for multiphase detonations. First, the effect of improved gas-phase chemistry will be explored utilizing global two-step chemistry for n-dodecane-air detonations. Next, the effect of localized reactions on droplets will be explored by utilizing a combined envelop burning and pure evaporation model for multiphase n-dodecane-oxygen detonations. As previously mentioned, current experimental work [31] is exploring pure oxygen combustion, from which a multitude of data is expected, such as average wave velocity, cellular structure, droplet positions in reference to the wave front and droplet lifetime estimates. The work previously conducted in [17] attempted to predict the multiphase detonation wave structure for different breakup models and droplet sizes, but lacked experimental validation.

This work found that localized equivalence ratios were perturbed by droplet lag, creating rich and lean areas for gas phase chemistry. To accurately model the reaction rates, a more advanced reaction model was needed. The first section of the results addresses this need by presenting the results from a two-step reaction model and comparing them to the previous one-step model. Air was used as the oxidizer in this study as two-step models more more readily available for such conditions and are more physically accurate under those regimes. Additionally, future work will target air detonations. The previous study also highlighted the effect of breakup on droplet evaporation rates, and that most vapor production occurred from small child droplets, which equilibrated rapidly with the gas flow. For these droplets, Reynolds numbers are sufficiently low that envelope burning may occur, increasing vapor productions rates. The second section of the results explores the effect of an envelop burning informed evaporation model, resulting in significantly faster vapor production rates for oxygen multiphase detonations in comparison to the previous work. Ideally, once experimental data becomes available, the particular model choices for gas phase reactions and droplet evaporation will be more clear.

3.1 Gaseous Detonations ($C_{12}H_{26} + 18.5[O_2 + 3.76N_2]$)

A prerequisite step for multiphase detonation simulations is confidence in gas phase reactions that will give reasonable results prior to the introduction of particles. This section will explore the results obtained from two-dimensional simulations utilizing the two-step global mechanism described in Section 2.3.3.2.

3.1.1 2-Step Global Mechanism

The simulation domain was initialized to be stoichiometric n-dodecane and air at atmospheric pressure and a temperature of 490 $[K]$. Three different grid resolutions were used to explore the length scales of the problem. The 1D distance to the CJ point is large in comparison with the ZND profile of the detonation. The results in Section 2.3.3.2 showed that the computed CJ point lies roughly 4 to 6 $[cm]$ behind the wave front while the ZND profile prediction places the peak thermicity at a distance of 443.2 [μm] behind the wave front and the exothermic pulse width at a distance of 250 [μm] centered around the peak thermicity. The highest desired resolution of the ZND profile for this study was approximately 5 discretizations within the exothermic pulse width (≈50 [μm]). Without prior knowledge of what the gaseous cell width is, the domain width was set to be y = 8 $[cm]$ because experiments with similar fuels [19] report structures on the order of

Δx_{min} $[\mu m]$	$D_{CJ,avg}$ $\times 10^{-2}$ $[cm/s]$
156.25	1959.0
78.13	1891.5
39.06	1873.8
GCI Analysis	
r	2
p^*_{scheme}	2
$p_{observed}$	1.93
GCI_{23}	2812.5 $[cm/s]$
GCI_{12}	737.5 $[cm/s]$
$r^p GCI_{12}/GCI_{23}$	1.05

Table 3.1: Average detonation velocity from 2D FLASH simulations utilizing the global 2-step mechanism with grid convergence index analysis. *It is assumed that the global order of accuracy in FLASH is limited by the PPM method being accurate to order 2 in time.

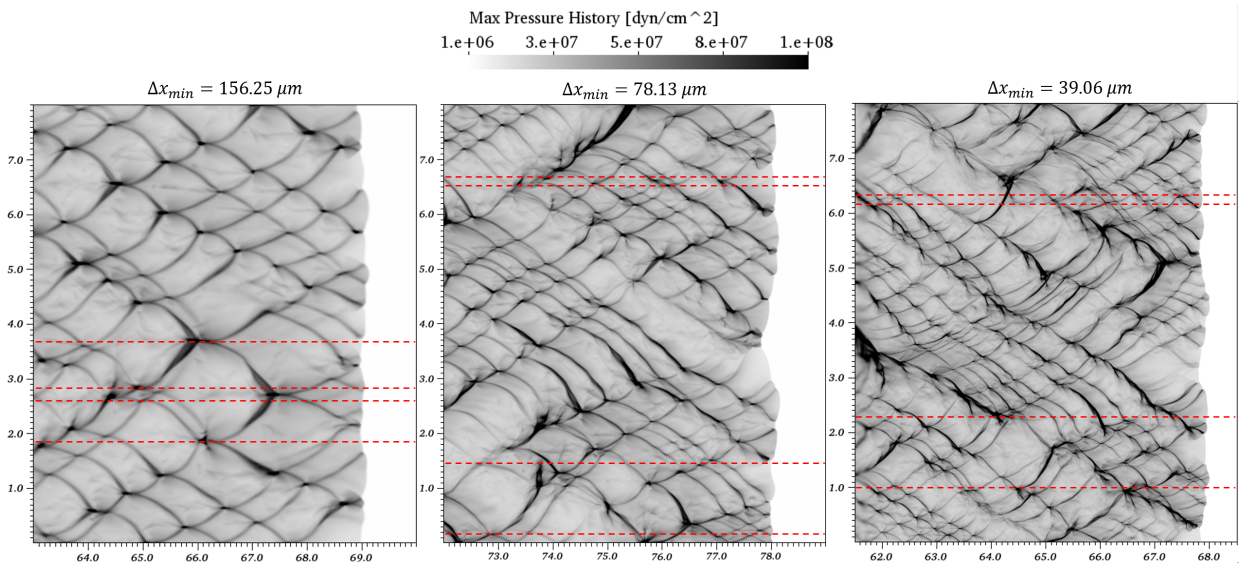

Figure 3.1: Numerical smoke foils for three different 2D simulations run using the general 2-step global reaction mechanism for a stoichiometric n-dodecane-air detonation. While exhibiting an irregular cellular structure, the largest and smallest observable features are on similar scales, dotted red lines for size comparison.

centimeters. FLASH is a block structured program with default divisions of 8 discretizations per block, thus, the minimum computational cell size when utilizing adaptive mesh refinement for a square mesh given maximum Level of Refinement (LoR) can be computed as $L_{Block}/(8 \cdot 2^{(LoR-1)})$. The domain was setup for one block in the y-direction for a square mesh using 7, 8, and 9 levels of refinement yielding minimum mesh sizes of 156.25, 78.13, and 39.06 $[\mu m]$, respectively. No restriction was put on the computation time step other than a maximum CFL number of 0.5.

Speeds in 2D were monitored over time and average propagation velocities can be seen in Table 3.1. Although not converged in the mesh sizes studied in this work, grid convergence index (GCI) analysis [86] yields an asymptotic ratio close to one, indicative of converging results. Detonations are unsteady by nature, which can make average speed analysis tricky given instantaneous fluctuation in propagation velocity can be on the order of $\pm 100 \cdot 10^2$ $[cm/s]$. Numerical reproductions of detonations often have higher speeds in higher space dimensions, as noted in [17], when comparisons are made to the 1D results obtained, e.g. the results obtained in Section 2.3.3.2. While not desirable, the differences in speed are often low enough ($\lesssim 5\%$) that the model is still believed to

give reasonable results. A difficulty this creates for multiphase detonation analysis is the necessity to quantify the average gaseous propagation speed at each mesh size studied so that fair $D_{CJ,avg}$ deficits can be quantified given that they can lie in a wide range from nearly no deficit to complete detonation failure.

Each simulation was run such that roughly 70 $[cm]$ of detonation cell history was obtained to observe the evolution over time. It can be seen in Figure 3.1 that the observed cellular structure is irregular for all resolutions studied, with an increase in irregularity as refinement increases. Although nothing definitive can be said for a regular cell width, qualitative assessment shows that the smallest and largest cellular features are of similar size in each simulation, putting confidence in the ability to resolve consistent cellular structures. Finer features of the detonation often lost when utilizing coarse grids can be seen in Figure 3.2, where decoupled shock fronts and reaction zones are visible in addition to isolated pockets of reactants falling behind the wave front, most clearly seen in the contour of CO_2.

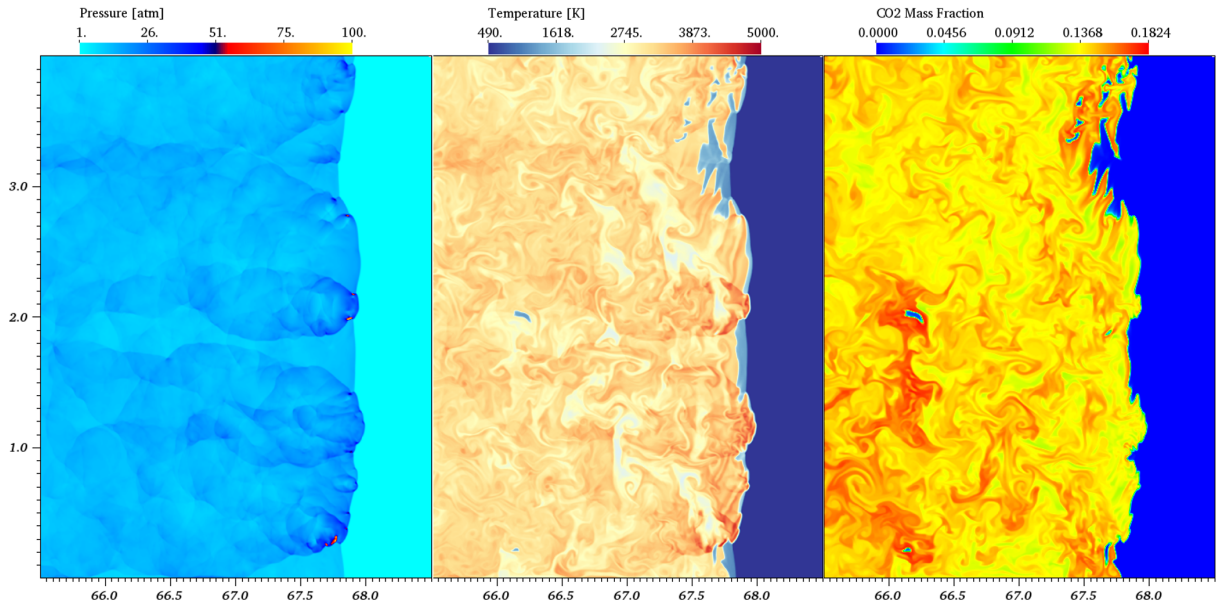

Figure 3.2: (Left) Pressure $[atm]$, (Center) temperature $[K]$, and (Right) CO_2 mass fraction contours from the 2-step global reaction mechanism. ($t = 350$ $[\mu s]$, $\Delta x_{min} = 39.06$ $[\mu m]$).

3.2 Multiphase Detonations ($C_{12}H_{26} + 18.5O_2$)

As discussed in Section 2.4.2.3, a combination of reduced order models was employed working under the assumption that wake burning occurs at $Re_{wake} \geq 270$ and envelope and/or boundary layer burning occurs beneath this limit. This GORBEH model was utilized under the exact same conditions for a previously run simulation in [17] for polydispersed 10 $[\mu m]$ droplets to compare the differences observed between evaporation models. The minimum grid resolution employed was 223.24 $[\mu m]$ with a forced maximum split-hydrodynamic time step of 2 $[ns]$ (4 $[ns]$ per full hydrodynamic time step) and two sub-steps per particle evolution time step.

3.2.1 Vaporization Effects

The major consequence inferred from the zero-dimensional results in Section 2.4.2.3 is that the GORBEH model will yield shorter droplet lifetimes, i.e. burning increases the mass production rate of a droplet. Figure 3.6 depicts particle relative velocities and Reynolds numbers at a late time in the simulation run. The transition from quiescent conditions to high velocity to equilibration with the gas flow can be seen in a relatively short space. The relative Reynolds number is artificially capped in the pseudocolor plot at the transition Reynolds number chosen for this simulation such that those droplets operating under the A-S model and those under the B_C combustion model can be visualized.

One of the first comparisons to known data that can be made is the average propagation velocity of the wave front. Taking the wave speed from the simulation run (see Figure 3.3) revealed that the detonation wave had a steady-state speed of $2133.3 \cdot 10^2$ $[cm/s]$, a 9.97% deficit from the gaseous speed of $2369.6 \cdot 10^2$ $[cm/s]$ (for the utilized grid size of 223 $[\mu m]$ in FLASH). In comparison with the previous case run utilizing Abramzon-Sirignano evaporation which had a average wave velocity of $2106.6 \cdot 10^2$ $[cm/s]$, the results match the intuition that with higher mass transfer rates, there should be less of a detonation wave deficit. The GORBEH evaporation model results in a 1.13% speedup in comparison with the A-S model.

As hypothesized in [17], it is believed that cell size should decrease with increased reaction

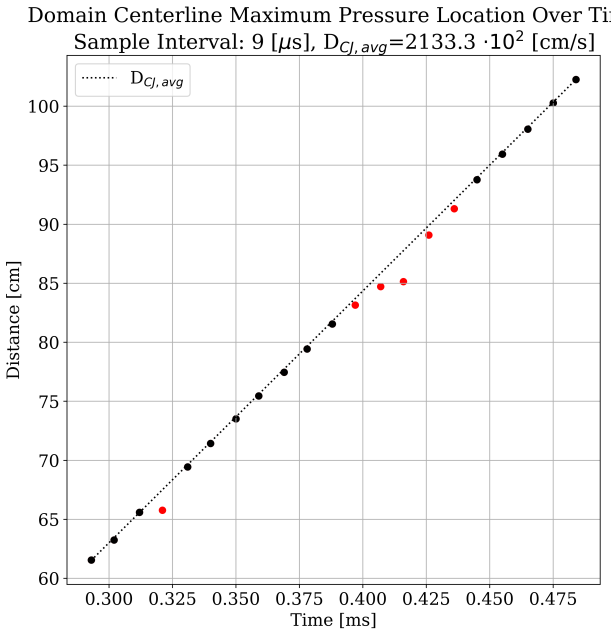

Figure 3.3: Maximum pressure locations in the domain centerline for late simulation times. $D_{CJ,avg}$ is obtained by sampling the maximum pressure locations in the center of the domain. The speed reported is taken from averaging the data points in black.

rates from vaporization. The numerical soot foil results obtained from the GORBEH model (see Figure 3.4) are smaller, and with similar regularity, to those obtained in the previous study, with an average cell width of $9.5\ [mm]$ in comparison to $12.7\ [mm]$. The numerical smoke foil from the previous study for polydispersed droplets can be seen in Figure A.1. For such a slight increase in propagation velocity, the GORBEH model has 6 regular cells across the domain width in comparison to the 4.5 obtained using the A-S model. Interestingly, the speed of the wave in this present work is significantly slower (2.84%) than that obtained in previous work for polydispersed $5\ [\mu m]$ droplets ($2195.6 \cdot 10^2\ [cm/s]$), however, the cellular structure is only slightly larger in comparison ($8.16\ [cm]$). A possible explanation for this could be variations in spatial equivalence ratios, both pre- and post-shock, as discussed in detail in [17].

One of the most important takeaways from [17] that had been noticed in other numerical works such as [37, 15] is that the post-shock conditions of the multiphase detonation are stratified with

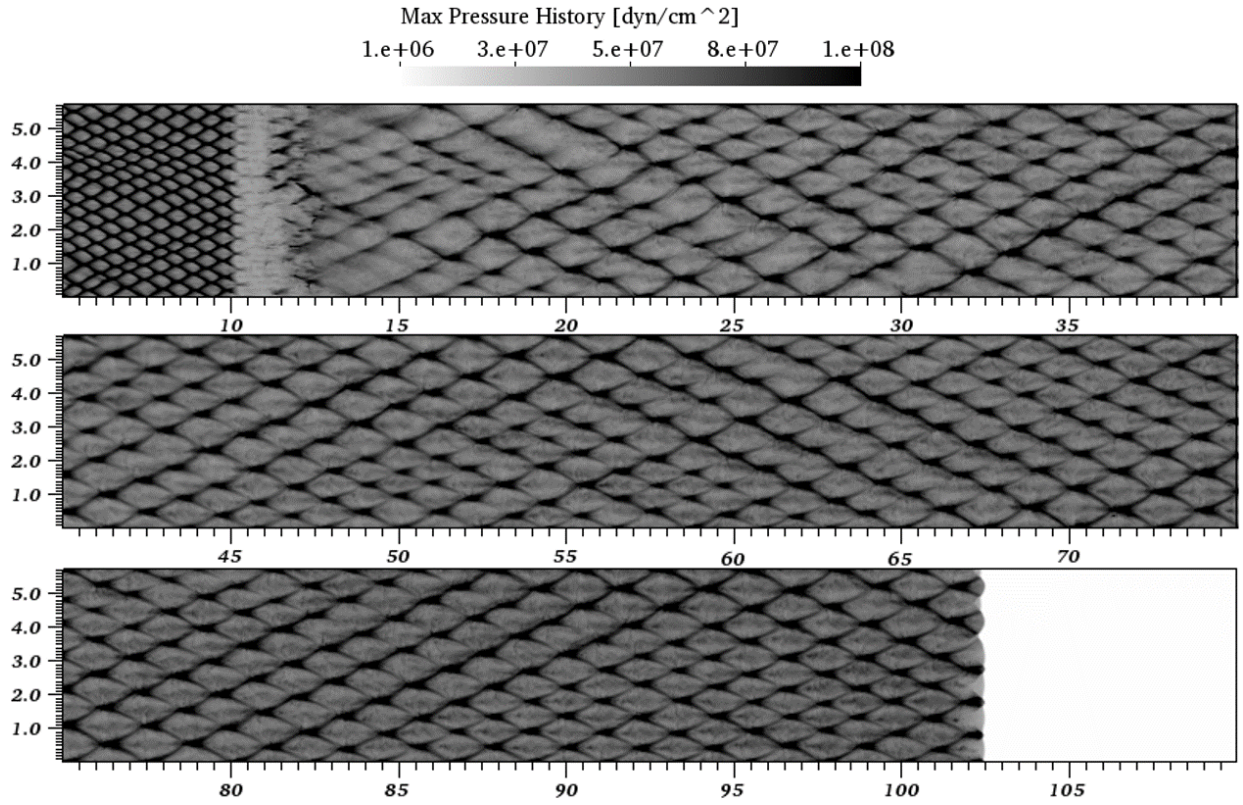

Figure 3.4: Numerical smoke foil results for the GORBEH vaporization model. The transition from gaseous premixed burning to droplet burning can be seen at 10 $[cm]$. The period of time until multiphase detonation stabilization is reached is dependent on the mass transfer model used; the visual transition to stability can be seen in the range of $x \approx 35 - 40$ $[cm]$.

regions of high and low fuel vapor concentration. If and when the fuel mixes with available oxidizer becomes a concern not often associated with premixed gaseous detonations. A visualization of this problem can be seen in Figure 3.5, where regions colored green and blue are spaces where the relative local Mach number ($D_{CJ,avg} - |\boldsymbol{u}|/a$) is less than one. This is an attempt to visualize the CJ plane in two spatial dimensions, but as seen in the figure, this is not a well defined region. While technically the area where useful burning, i.e. contributing to the wave propagation, is occurring, this may not hold true in 2D, especially in regions of $Ma < 1$ that have become disconnected from the continuous region directly behind the wavefront.

Without a clearly defined CJ plane in 2D, the alternative is to quantify where useful burning is occurring in more than one dimension, such as the work conducted in [87] that concluded regions

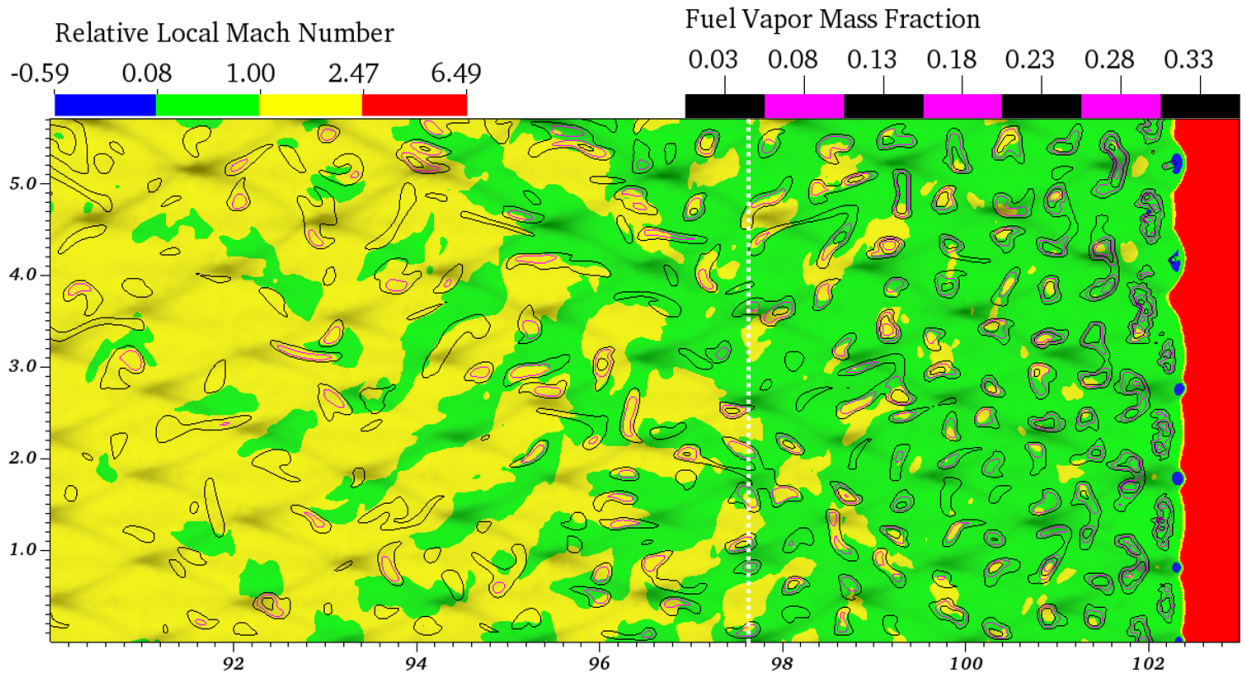

Figure 3.5: Relative Mach number plot with fuel vapor mass fraction contours. Local Mach number is in reference to $D_{CJ,avg}$. Plotted at $t = 484\ [\mu s]$. Cellular structure overlaid with white dashed line placed approximately at two cell lengths for reference.

capable of influencing the detonation are one to two cells lengths behind the front, the numerical soot foil is overlaid in Figure 3.5 for reference. Fuel vapor mass fraction contours can be seen in the same plot to provide context for which groups of fuel may not ever contribute to the wave front. A magnified pseudocolor plot of fuel vapor mass fraction can also be seen in Figure 3.7.

3.3 Takeaways

The sensitivity of detonation properties to the particular models employed for reactions and droplet mass transfer is high, with varying degrees of observable differences and physical significance. Two important aspects of reproducing numerical detonations were investigated in this work: gas phase and droplet combustion. While the two-step global mechanism is not applicable for pure oxygen combustion, the post-shock and CJ conditions obtained for air combustion were reasonable when comparing to physical predictions. The two-step mechanism is likely to perform best in lean equivalence ratio regimes where the variation in end state from detailed mechanisms is

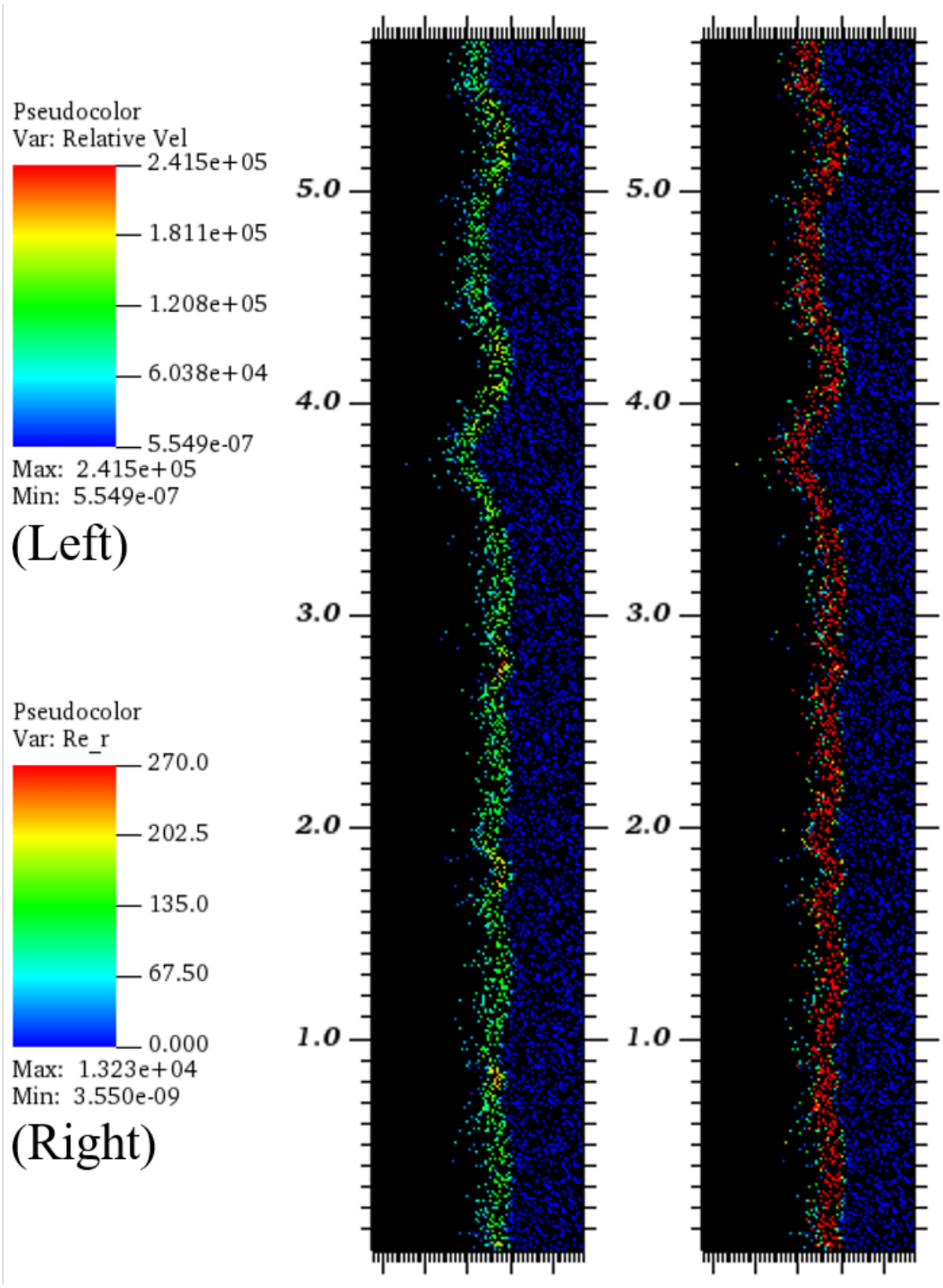

Figure 3.6: (Left) Relative velocity $[cm/s]$ and (Right) relative Reynolds number (pseudocolor plot capped at $Re = Re_{wake} = 270$) from the GORBEH vaporization model results at $t = 484$ $[\mu s]$. All droplets with Reynolds numbers above Re_{wake} utilize the A-S vaporization model while those below, and able to burn, utilize the combustion model.

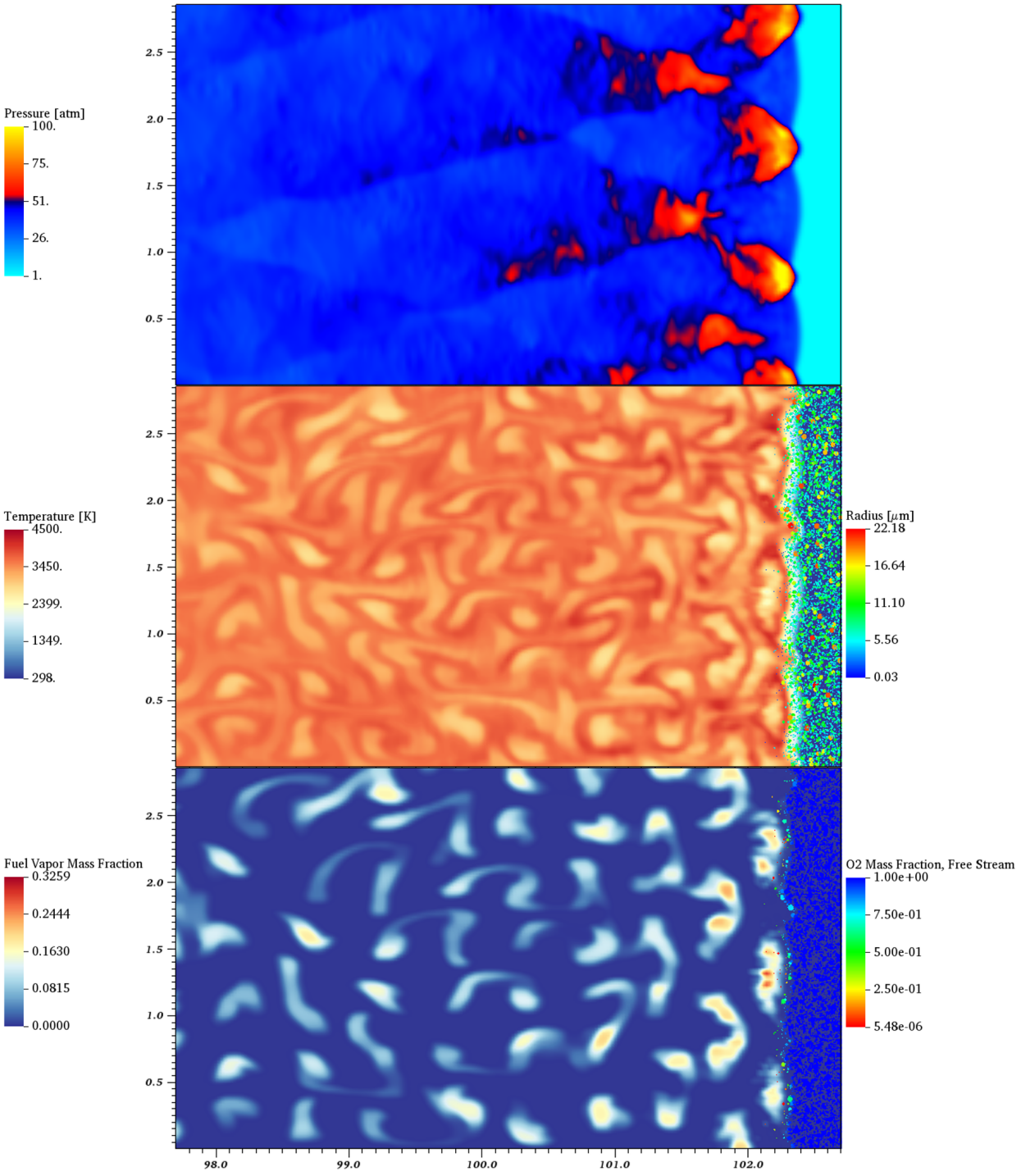

Figure 3.7: (Top) Pressure $[atm]$, (Center) temperature $[K]$, and (Bottom) fuel mass fraction contours from the GORBEH vaporization model at $t = 484$ $[\mu s]$. Particle positions are plotted with pseudocolors for (Center) radius $[cm]$ and (Bottom) free stream oxygen mass fraction.

low. Such a mechanism should perform well in stratified flow conditions, e.g. where particles are clustering, assuming the correction functions are tuned appropriately for the chosen fuel. Here the functions used were taken from the BFER kerosene mechanism but other fuels are readily available, e.g. methane [81]. For the evaporation models examined, model choice proved to have less of an impact on multiphase detonation than the choice of a breakup model. Despite having less of an impact, the observable effect was still measurable, having quantifiable differences in propagation velocities and 2D cellular structure. Localized reaction effects increased the vapor production and reaction rate from droplets after breakup, leading to an overall faster detonation wave.

4. SUMMARY AND CONCLUSIONS

This work examined two major aspects of detonation modeling: global reaction mechanisms for detonation reproduction and the impact of a combustion informed vaporization model on the propagation of a multiphase detonation. A generalized two-step global reaction mechanism was found to be acceptable for air detonations and likely applicable multiphase detonation modeling. The sensitivity of a multiphase detonation to vaporization models was quantified in comparison to an existing results utilizing an evaporation model agnostic to combustion. Unlike the study of [17] which showed the difference between two breakup models can yield extremely different results, the difference between the two evaporation models was measurable, but small in comparison to the effect of breakup models. In conclusion, this work can be summarized in the following points:

- The capabilities of the open-source FLASH hydrodynamics code have been expanded to include a general two-step, global chemical reaction mechanism for hydrocarbon combustion and a combustion informed droplet vaporization model.
- It is essential that gas phase chemistry models be capable of operating in a wide range of equivalence ratios for accurate multiphase detonation modeling given the inherent stratified flow conditions.
- Mass transfer rates informed of localized droplet combustion will impact the numerical multiphase detonation with quantifiable differences in wave propagation velocity and cellular structure.

As shown in works such as [15, 17], global one-step mechanisms are perfectly capable of reproducing believable detonations. One of the biggest uncertainties surrounding them is how accurate are the results obtained from using such a mechanism when they are only tuned for one specific condition with one thermodynamic end state in mind. In an attempt to minimize the amount of tuning involved with such mechanisms, a generalized two-step mechanism was proposed based on

the concepts discussed in [77, 82] that is no longer dependent on a tuned product composition and aware of different localized burning conditions. Such a mechanism appears to yield appropriate results for air combustion given a fine enough resolution is employed to resolve the structure of the detonation wave.

Reduced order modeling is a major tool employed for Euler-Lagrange simulations attempting to resolve the physics of millions of particle points in a realistic and computationally efficient manner. The time scales of such models become increasingly important as the desired results become directly dependent on their prediction. Explored in [17], the choice of a breakup model can either yield a complete multiphase detonation failure or a nearly gaseous detonation. The effect of changing the evaporation model in this study is not as impactful as changing the breakup model, but still gave significant quantitative differences observed in steady state propagation velocity and cellular detonation structure.

4.1 Challenges

Currently, the major challenge surrounding the multiphase detonation phenomena is a lack of comparison data for validation, especially for low vapor pressure fuels. There are two different approaches that need to be taken for proper Euler-Lagrange model validation: experimental data from multiphase detonations and droplet lifetime history from shocked droplets. From the perspective of detonation experiments, steady (or lack thereof) propagation velocities and cellular structures, such as the data in [27, 28], are required for a wide range of fuels and initial conditions. Droplet evolution under strong shock conditions needs to be well documented if reduced order models aim to reproduce accurate time scales for events such as breakup and evaporation. Works such as [51, 53] have investigated droplet evolution under strong shock conditions for high vapor pressure substances attempting to provide time scales for total droplet lifetime and zone of influence. Other work such as [54] is attempting to quantify the evolution of low vapor pressure fuels under low, strong, and detonation shock strengths which should provide enormous insight into the fundamental physics at play in multiphase detonations. However, an aspect not covered by the mentioned studies is that systems where the propagation of a reaction front is dependent on fuel vaporization

also need to be investigated with the same level of detail. Simply put, measurements of droplet morphology, drag, breakup/evaporation rates, and child droplet sizes are needed for relevant multiphase detonation conditions. Additionally, to confidently use reduced order evaporation models informed on burning conditions, such as the GORBEH model presented in this work, experimental data is required to quantify the flame structure under low, high, detonation and multiphase detonation conditions.

4.2 Further Study

A key aspect often neglected in the study of detonations is the three-dimensionality of the problem. The assumption of symmetry in the third dimension is likely giving artificial stability to the cellular structures observed in the results presented in this work and other similar studies. Given that cellular structure is one of the easiest aspects of detonations to quantify, the structure obtained in 3D may be required for final code validation.

The next logical step in reaction chemistry would be the implementation of the global mechanism detailed in [79] which has the potential to produce physical results for both air and oxygen combustion regimes. The model may need correction factors for equivalence ratio incorporated in a similar way to the BFER kerosene mechanism [82]. Eventually, models will need to be perfected for air detonation conditions as the end use application for these models is likely in the propulsion field, i.e. air-breathing engines. Without information about the specific burning conditions, e.g. oxygen enriched conditions or low pressure environments, and especially considering the stratification of fuel vapor concentration inherent to multiphase detonations, the ability to utilize one general mechanism that reliably and accurately predicts reactions and thermodynamic states in the gas phase would allow for more attention (or scrutiny) to be applied to the heat and mass transfer models surrounding the droplets.

As previously mentioned, one of the major challenges surrounding numerical modeling of multiphase detonations is the lack of data available for validation. A key focus of current work at the FMECL facility is detonation propagation feasibility in low vapor pressure fuels. As experimental data for detonations propagating through liquid fuels such as decane, dodecane, kerosene/RP-2,

or JP-10 become available, more points of comparison can be made to improve different aspects of numerical modeling. An immediate step that can be taken towards validation is conducting a numerical study to match one or several of the experiments detailed in [16, 26, 24]. The experiments in question detail detonations with the higher hydrocarbon liquid fuels octane, decane, and dodecane at various equivalence ratios and artificial laboratory air compositions. Successful detonations were obtained consistently with octane while irregular and spinning regimes were found for stoichiometric decane- and dodecane-air detonations with relatively low droplet sizes ($8\ [\mu m]$). Soot foils are available from these experiments for qualitative assessment. Detonations were unsuccessful with larger droplet sizes of $30\ [\mu m]$ and $45\ [\mu m]$. With a similar laboratory setup present in the FMECL facility [31], an attempt could be made to obtain comparable experimental data to add to the certainty of the observed regimes. Application of the global two-step mechanism tuned for different equivalence ratios in addition to the available vaporization models would allow for a physical point of comparison, taking a leap towards code validation.

REFERENCES

[1] D. G. Goodwin, H. K. Moffat, and R. L. Speth, "Cantera: An object-oriented software toolkit for chemical kinetics, thermodynamics, and transport processes." `http://www.cantera.org`, 2017. Version 2.3.0.

[2] E. D. Laboratory, "Shock and detonation toolbox." `https://shepherd.caltech.edu/EDL/PublicResources/sdt/`, 2021.

[3] H. Wang, E. Dames, B. Sirjean, D. A. Sheen, R. Tango, A. Violi, J. Y. W. Lai, F. N. Egolfopoulos, D. F. Davidson, R. K. Hanson, C. T. Bowman, C. K. Law, W. Tsang, N. P. Cernansky, D. L. Miller, and R. P. Lindstedt, "A high-temperature chemical kinetic model of n-alkane (up to n-dodecane), cyclohexane, and methyl-, ethyl-, n-propyl and n-butyl-cyclohexane oxidation at high temp+s, jetsurf version 2.0." `http://web.stanford.edu/group/haiwanglab/JetSurF/JetSurF2.0/index.html`, 2010.

[4] K. Kailasanath, *Recent Developments in the Research on Pressure-Gain Combustion Devices*, pp. 3–21. Singapore: Springer Singapore, 2020.

[5] D. L. C. B. (Oxon.), "Vi. on the rate of explosion in gases," *Lond. Edinb. Dublin Philos. Mag.*, vol. 47, no. 284, pp. 90–104, 1899.

[6] E. Jouguet, "Sur la propagation des réactions chimiques dans les gaz [on the propagation of chemical reactions in gases]," *J. Math Pure Appl.*, vol. 6, no. 1, pp. 347–425, 1905.

[7] E. Jouguet, "Sur la propagation des réactions chimiques dans les gaz [on the propagation of chemical reactions in gases]," *J. Math Pure Appl.*, vol. 6, no. 2, pp. 5–85, 1906.

[8] Y. Zel'dovich, "On the theory of the propagation of detonations on gaseous system," *J. Exp. Theor. Phys+*, vol. 10, pp. 542–568, 1940.

[9] J. von Neumann, *Theory of detonation waves. Progress Report to the National Defense Research Committee Div. B*, p. 178–218. OSRD-549 (PB 31090), New York: Pergamon Press,

1942.

[10] W. Döring, "Über detonationsvorgang in gasen," *Ann. Phys.*, vol. 43, pp. 421–436, 1943.

[11] F. Pintgen and J. Shepherd, "Simultaneous soot foil and plif imaging of propagating detonations," in *19th ICDERS*, 2003.

[12] K. Kailasanath, E. Oran, J. Boris, and T. Young, "Determination of detonation cell size and the role of transverse waves in two-dimensional detonations," *Combust. Flame*, vol. 61, no. 3, pp. 199–209, 1985.

[13] J. H. S. Lee, *The Detonation Phenomenon*. Cambridge University Press, 2008.

[14] S. Cheatham and K. Kailasanath, "Numerical modelling of liquid-fuelled detonations in tubes," *Combust. Theor. Model*, vol. 9, no. 1, pp. 23–48, 2005.

[15] D. A. Schwer, "Multi-dimensional simulations of liquid-fueled jp10/oxygen detonations," *AIAA Prop. and Energ. 2019 Forum*, pp. 1–18, 2019.

[16] B. Veyssiere, B. Khasainov, M. Mar, and M. Benmahammed, "Investigation of detonation propagation regimes in liquid sprays," in *24th ICDERS*, 2013.

[17] B. Musick, M. Paudel, J. McFarland, and P. Ramaprabhu, "Numerical simulations of droplet evaporation and breakup effects on heterogeneous detonations," *[Manuscript submitted for publication] Department of Mechanical Engineering, Texas A&M University*, 2023.

[18] J. Shepherd, "Detonation in gases," *Proc. Combust. Inst.*, vol. 32, no. 1, pp. 83–98, 2009.

[19] J. Austin and J. Shepherd, "Detonations in hydrocarbon fuel blends," *Combustion and Flame*, vol. 132, no. 1, pp. 73–90, 2003.

[20] N. Chaumeix, B. Imbert, L. Catoire, and C. E. Paillard, "The onset of detonation behind shock waves of moderate intensity in gas phase," *Combustion Science and Technology*, vol. 186, no. 4-5, pp. 607–620, 2014.

[21] K. Kailasanath, "Liquid-fueled detonations in tubes," *J. Propul. Power*, vol. 22, no. 6, pp. 1261–1268, 2006.

[22] P. Lu, N. Slagg, B. Fishburn, and P. Ostrowski, "Relation of chemical and physical processes in two-phase detonations," *Acta. Astronaut.*, vol. 6, no. 7, pp. 815–826, 1979.

[23] S. M. Frolov, V. Y. Basevich, V. S. Aksenov, and S. A. Polikhov, "Detonation initiation in liquid fuel sprays by successive electric discharges," *Doklady Physical Chemistry*, vol. 394, pp. 39–41, 2004.

[24] M. A. Benmahammed, B. Veyssiere, B. A. Khasainov, and M. Mar, "Effect of gaseous oxidizer composition on the detonability of isooctane–air sprays," *Combust. Flame*, vol. 165, pp. 198–207, 2016.

[25] D. C. Bull, M. A. McLeod, and G. A. Mizner, *Detonation of Unconfined Fuel Aerosols*, pp. 48–60. 1979.

[26] M. E.-A. Benmahammed, *Détonations dans les aérosols de gouttelettes liquides réactives. Etude de l'influence des propriétés physicochimiques de la phase liquide et de l'oxydant gazeux*. PhD thesis, Poitiers, France, 2013.

[27] M. Tang, J. Nicholls, M. Sichel, and Z. Lin, "The direct initiation of detonation in decane-air and decane-oxygen sprays," tech. rep., Ann Arbor, Michigan, 1983.

[28] J. Papavassiliou, A. Makris, R. Knystautas, J. H. Lee, C. K. Westbrook, and W. J. Pitz, *Measurements of Cellular Structure in Spray Detonation*, pp. 148–169. 1991.

[29] V. Alekseev, S. Dorofeev, V. Sidorov, and B. Chaivanov, *Experimental Study of Large-Scale Unconfined Fuel Spray Detonations*, pp. 95–104. 1993.

[30] J. Kindracki, "Study of detonation initiation in kerosene–oxidizer mixtures in short tubes," *Shock Waves*, vol. 24, pp. 603–618, 2014.

[31] C. Young, "Development of a multiphase detonation tube," Master's thesis, Texas A&M University, 2022.

[32] S. Eidelman and A. Burcat, "Evolution of a detonation wave in a cloud of fuel droplets: Part i. influence of igniting explosion," *AIAA J.*, vol. 18, pp. 1103–1108, 1980.

[33] A. Burcat and S. Eidelman, "Evolution of a detonation wave in a cloud of fuel droplets: Part ii. influence of fuel drops," *AIAA J.*, vol. 18, pp. 1233–1236, 1980.

[34] S. Eidelman and A. Burcat, "The mechanism of a detonation wave enhancement in a two-phase combustible medium," *Symp. (Int.) Combust.*, vol. 18, no. 1, pp. 1661–1670, 1981. Eighteenth Symp Combust Proc.

[35] D. Voronin and S. Zhdan, "Calculation of heterogeneous detonation initiation for a hydrogen-oxygen mixture in an explosion tube," *Combust. Explo. Shock+*, vol. 20, no. 4, pp. 461–465, 1984.

[36] H. Shen, G. Wang, K. Liu, and D. Zhang, "Numerical simulation of liquid-fueled detonations by an eulerian–lagrangian model," *Int. J. Nonlin. Sci. Num.*, vol. 13, no. 2, pp. 177–188, 2012.

[37] D. A. Schwer, J. Eugene P. O'Fallon, and D. A. Kessler, "Liquid-fueled detonation modeling at the u.s. naval research laboratory," tech. rep., Naval Research Laboratory, Washington, DC 20375-5320, 2018.

[38] A. K. Hayashi, N. Tsuboi, and E. Dzieminska, "Numerical study on jp-10/air detonation and rotating detonation engine," *AIAA J.*, vol. 58, no. 12, pp. 5078–5094, 2020.

[39] Z. Huang, M. Zhao, Y. Xu, G. Li, and H. Zhang, "Eulerian-lagrangian modelling of detonative combustion in two-phase gas-droplet mixtures with openfoam: Validations and verifications," *Fuel*, vol. 286, p. 119402, 2021.

[40] Q. Meng, M. Zhao, H. Zheng, and H. Zhang, "Eulerian-lagrangian modelling of rotating detonative combustion in partially pre-vaporized n-heptane sprays with hydrogen addition," *Fuel*, vol. 290, p. 119808, 2021.

[41] Q. Meng, N. Zhao, and H. Zhang, "On the distributions of fuel droplets and in situ vapor in rotating detonation combustion with prevaporized n-heptane sprays," *Phys. Fluids.*, vol. 33, p. 043307, 2021.

[42] M. Zhao and H. Zhang, "Numerical simulation of two-dimensional detonation propagation in partially pre-vaporized n-heptane sprays," *ICLASS Edinburgh: Fuel Sprays & Combustion*, vol. 1, pp. 1–8, 2021.

[43] X.-Y. Liu, M.-Y. Luan, Y.-L. Chen, and J.-P. Wang, "Propagation behavior of rotating detonation waves with premixed kerosene/air mixtures," *Fuel*, vol. 294, p. 120253, 2021.

[44] M. Salvadori, A. Panchal, D. Ranjan, and S. Menon, *Numerical Study of Detonation Propagation in H2-air with Kerosene Droplets*.

[45] P. J. O'rourke and A. A. Amsden, "The tab method for numerical calculation of spray droplet breakup," 1987.

[46] C. Crowe, J. Schwarzkopf, M. Sommerfeld, and Y. Tsuji, *Multiphase Flows with Droplets and Particles*. CRC Press, 2011.

[47] E. Michaelides, C. Crowe, and J. Schwarzkopf, *Multiphase Flow Handbook*. CRC Press, 2 ed., 2016.

[48] B. Abramzon and W. Sirignano, "Droplet vaporization model for spray combustion calculations," *Int. J. Heat Mass Tran.*, vol. 32, pp. 1605–1618, 1989.

[49] K. Wert, "A rationally-based correlation of mean fragment size for drop secondary breakup," *Int. J. Multiphas. Flow*, vol. 21, no. 6, pp. 1063–1071, 1995.

[50] J. Char, W. Liou, and J. Yeh, "Ignition and combustion study of jp-8 fuel in a supersonic flowfield," *Shock Waves*, vol. 6, pp. 259–266, 1996.

[51] A. Kobiera, J. Szymczyk, P. Wolański, and A. Kuhl, "Study of the shock-induced acceleration of hexane droplets," *Shock Waves*, vol. 18, no. 6, pp. 475–485, 2009.

[52] V. Duke-Walker, W. C. Maxon, S. R. Almuhna, and J. A. McFarland, "Evaporation and breakup effects in the shock-driven multiphase instability," *J. Fluid Mech.*, vol. 908, p. A13, 2021.

[53] V. Duke-Walker, B. J. Musick, and J. A. McFarland, "Experiments on the breakup and evaporation of small droplets at high weber number," *Int. J. Multiphas. Flow*, vol. 161, p. 104389, 2023.

[54] S. Salauddin, A. J. Morales, R. Hytovick, R. Burke, V. Malik, J. Patten, S. Schroeder, and K. A. Ahmed, "Detonation and shock-induced breakup characteristics of rp-2 liquid droplets," *Shock Waves*, 2023.

[55] A. Liu, D. Mather, and R. Reitz, "Modeling the effects of drop drag and breakup on fuel sprays," *SAE Tech. Paper 930072*, p. 17, 03 1993.

[56] J. C. Beale and R. D. Reitz, "Modeling spray atomization with the kelvin-helmholtz/rayleigh-taylor hybrid model," *Atomization Spray*, vol. 9, no. 6, pp. 623–650, 1999.

[57] S. Sharma, A. Pratap Singh, S. Srinivas Rao, A. Kumar, and S. Basu, "Shock induced aero-breakup of a droplet," *Journal of Fluid Mechanics*, vol. 929, p. A27, 2021.

[58] T. Theofanous and G. Li, "On the physics of aerobreakup," *Phys. Fluids.*, vol. 20, p. 052103, 05 2008.

[59] T. Theofanous, "Aerobreakup of newtonian and viscoelastic liquids," *Annu. Rev. Fluid Mech.*, vol. 43, no. 1, pp. 661–690, 2011.

[60] G. Godsave, "Studies of the combustion of drops in a fuel spray—the burning of single drops of fuel," *Symp. (Int.) Combust.*, vol. 4, no. 1, pp. 818–830, 1953. Fourth Symp Combust Proc.

[61] S. R. Gollahalli and T. Brzustowski, "Experimental studies on the flame structure in the wake of a burning droplet," *Symposium (International) on Combustion*, vol. 14, no. 1, pp. 1333–1344, 1973. Fourteenth Symposium (International) on Combustion.

[62] Y. Zhang, Y. Yang, Y. Wei, and S. Liu, "Vortex shedding controlled combustion of the wake flame of an n-heptane wetted porous sphere," *AIP Advances*, vol. 12, 10 2022. 105216.

[63] H.-H. Chiu and J.-S. Huang, "Multiple-state phenomena and hysteresis of a combusting isolated droplet," *Atomization and Sprays*, vol. 6, no. 1, pp. 1–26, 1996.

[64] H. Chiu, "Advances and challenges in droplet and spray combustion. i. toward a unified theory of droplet aerothermochemistry," *Progress in Energy and Combustion Science*, vol. 26, no. 4, pp. 381–416, 2000.

[65] S. S. Sazhin, *Droplets and Sprays: Simple Models of Complex Processes*. Springer Cham, 2023.

[66] B. Fryxell, K. Olson, P. Ricker, F. X. Timmes, M. Zingale, D. Q. Lamb, P. MacNeice, R. Rosner, J. W. Truran, and H. Tufo, "FLASH: An adaptive mesh hydrodynamics code for modeling astrophysical thermonuclear flashes," *The Astrophysical Journal Supplement Series*, vol. 131, pp. 273–334, nov 2000.

[67] P. MacNeice, K. M. Olson, C. Mobarry, R. deFainchtein, and C. Packer, "Paramesh: A parallel adaptive mesh refinement community toolkit," tech. rep., NASA, Greenbelt, Maryland 20771, 1999.

[68] M. J. Andrews and P. J. O'rourke, "The multiphase particle-in-cell (mp-pic) method for dense particulate flows," *Int. J. Multiphas. Flow*, vol. 22, pp. 379–402, 1996.

[69] D. M. Snider, S. M. Clark, and P. J. O'Rourke, "Eulerian–lagrangian method for three-dimensional thermal reacting flow with application to coal gasifiers," *Chem. Eng. Sci.*, vol. 66, no. 6, pp. 1285–1295, 2011.

[70] J. Dahal and J. A. McFarland, "A numerical method for shock driven multiphase flow with evaporating particles," *J. Comput. Phys.*, vol. 344, pp. 210–233, 2017.

[71] P. Colella and P. R. Woodward, "The piecewise parabolic method (ppm) for gas-dynamical simulations," *J. Comput. Phys.*, vol. 54, no. 1, pp. 174–201, 1984.

[72] E. S. Oran and J. P. Boris. Cambridge University Press, 2 ed., 2000.

[73] D. C. Horning, *A Study of the High-Temperature Autoignition and Thermal Decomposition of Hydrocarbons*. PhD thesis, Stanford, California 94305-3032, 2001.

[74] M. Paudel, "Numerical study of shock driven multiphase systems with reactions," *University of Missouri*, 2018.

[75] F. Perini, E. Galligani, and R. D. Reitz, "An analytical jacobian approach to sparse reaction kinetics for computationally efficient combustion modeling with large reaction mechanisms," *Energy & Fuels*, vol. 26, no. 8, pp. 4804–4822, 2012.

[76] F. Timmes, "Integration of nuclear reaction networks for stellar hydrodynamics," *THE ASTROPHYSICAL JOURNAL SUPPLEMENT SERIES*, vol. 124, pp. 241–263, 1999.

[77] C. K. Westbrook and F. L. Dryer, "Simplified reaction mechanisms for the oxidation of hydrocarbon fuels in flames," *Combust. Sci. Technol.*, vol. 27, no. 1-2, pp. 31–43, 1981.

[78] E. Schultz and J. Shepherd, "Validation of detailed reaction mechanisms for detonation simulation," 2000.

[79] D. J. Singh and C. J. Jachimowski, "Quasiglobal reaction model for ethylene combustion," *AIAA Journal*, vol. 32, no. 1, pp. 213–216, 1994.

[80] M. Sichel, N. A. Tonello, E. S. Oran, and D. A. Jones, "A two-step kinetics model for numerical simulation of explosions and detonations in h2-o2 mixtures," *Proceedings: Mathematical, Physical and Engineering Sciences*, vol. 458, no. 2017, pp. 49–82, 2002.

[81] B. Franzelli, E. Riber, L. Y. Gicquel, and T. Poinsot, "Large eddy simulation of combustion instabilities in a lean partially premixed swirled flame," *Combustion and Flame*, vol. 159, no. 2, pp. 621–637, 2012.

[82] B. Franzelli, E. Riber, M. Sanjosé, and T. Poinsot, "A two-step chemical scheme for kerosene–air premixed flames," *Combustion and Flame*, vol. 157, no. 7, pp. 1364–1373, 2010.

[83] D. Spalding, "A standard formulation of the steady convective mass transfer problem," *Int. J. Heat Mass Tran.*, vol. 1, pp. 192–207, Aug. 1960.

[84] R. Clift, J. R. Grace, and M. E. Weber, *Bubbles, Drops, and Particles*. Academic Press, 1978.

[85] A. H. Lefebvre, *Atomization and sprays*. CRC Press, 1988.

[86] P. J. Roache, "Perspective: A Method for Uniform Reporting of Grid Refinement Studies," *J. Fluid Eng.-T ASME*, vol. 116, pp. 405–413, 09 1994.

[87] V. Gamezo, D. Desbordes, and E. Oran, "Two-dimensional reactive flow dynamics in cellular detonation waves," *Shock Waves*, vol. 9, no. 1, p. 11–17, 1999.

APPENDIX A

COMPARISON DATA[1]

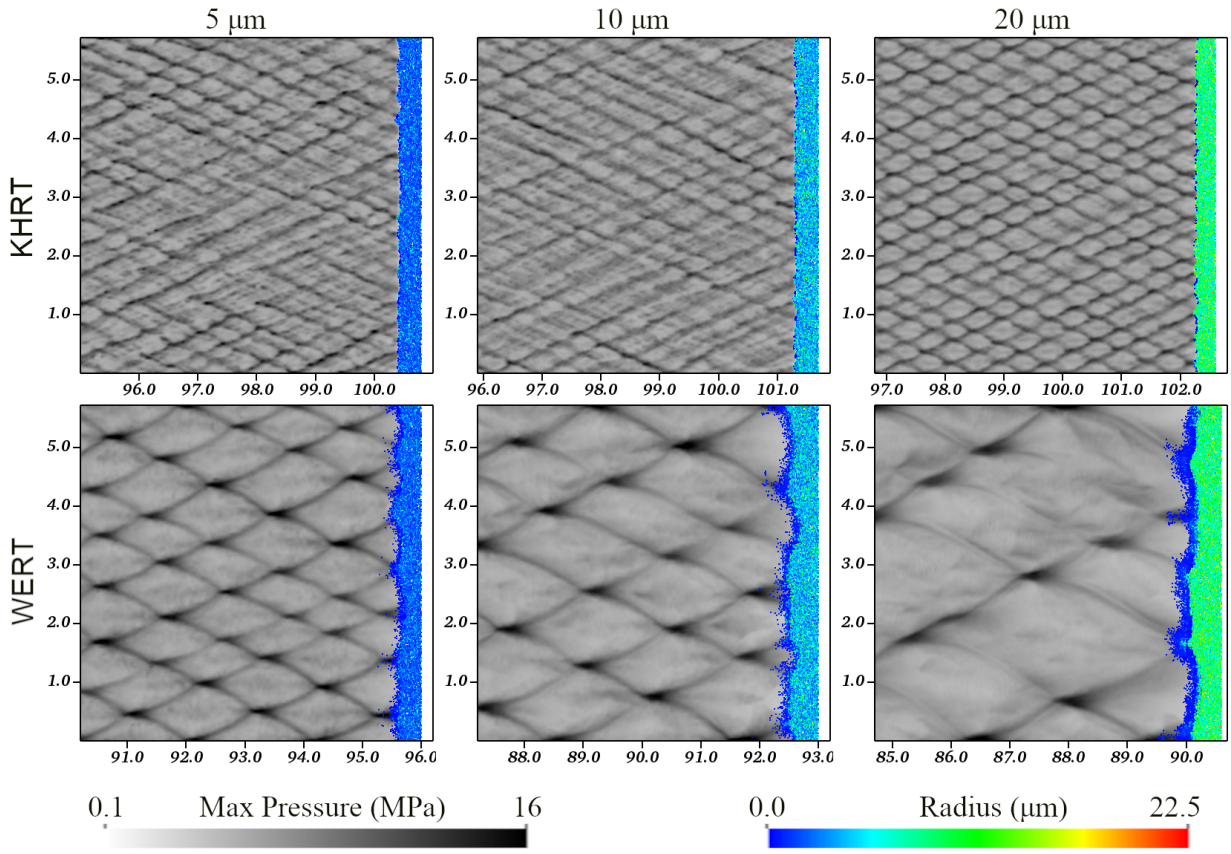

Figure A.1: Numerical smoke foil history for the polydispersed sprays studied in previous work. Reproduced with permission from [17].

[1]Parts of this chapter are reprinted with permission from [17].

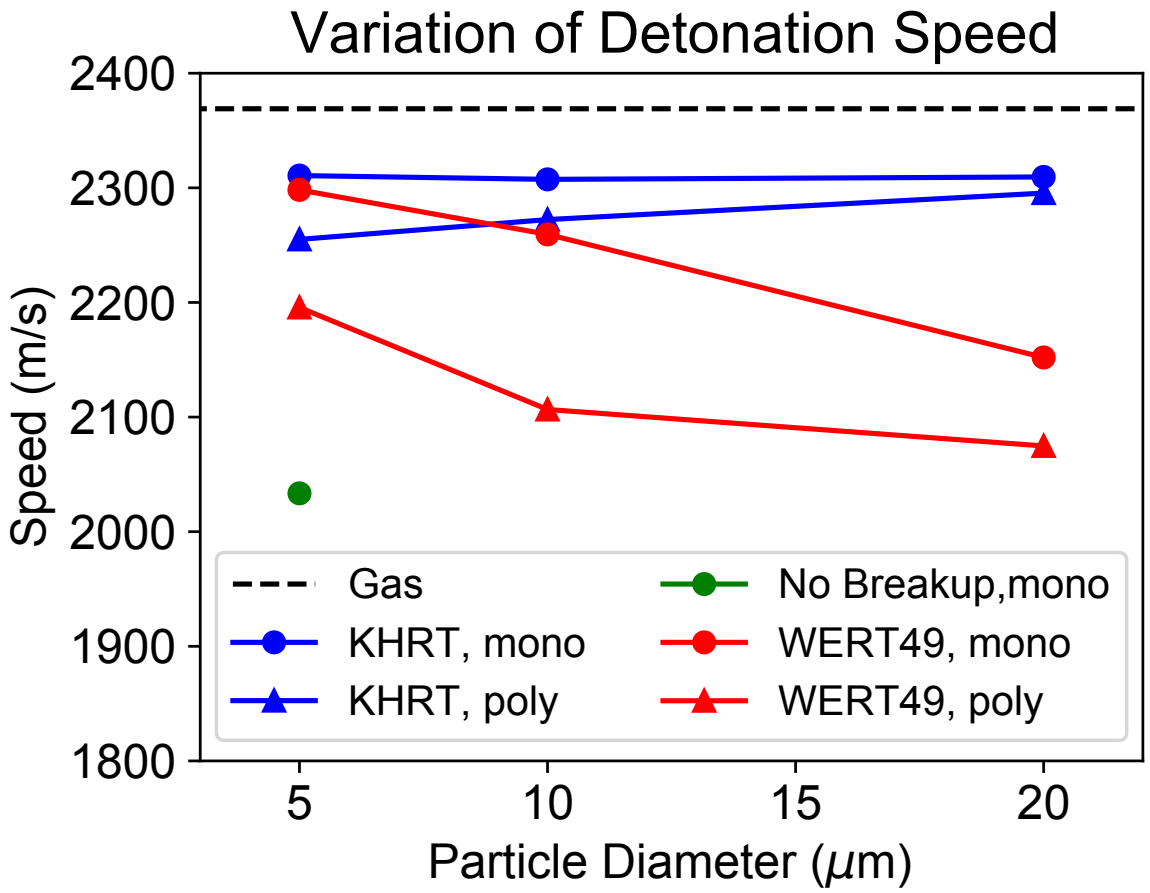

Figure A.2: Multiphase detonation speeds from monodispersed sprays with and without breakup and polydispersed sprays with breakup. Reproduced with permission from [17].